CHAPTER 3
Exciton Transition Energy and Bowing Parameter of AlGaN Alloys

3. 1 INTRODUCTION

GaN and its heterostructure with AlGaN have attracted much attention to fabricate high power/high speed heterojunction field-effect transistors[1] as well as near UV laser diodes[2] and vision-blind UV detectors.[3] In such device applications, a crucial property of the AlGaN alloys is the composition dependence of the band gap energy (E_g), which is described by a linear behavior of Al mole fraction (x) and a nonlinear deviation of bowing parameter (b). Up to now, a number of investigations have been done on the determination of the two parameters x and b.[4] Although the composition of AlGaN alloys obtained by chemical evaluation methods, such as electron probe micro analysis (EPMA) or Rutherford-backscattering spectrometry (RBS), etc., is considered more accurate than that extracted from the measurement of X-ray diffraction (XRD), it was suggested recently that with taking account of the in-plane biaxial strain effect on both lattice parameters, a and c, the XRD method is also possible to generate precise Al content and, furthermore, provides information about the microstructure of epitaxial layers.[5] On the other hand, for the bowing parameter, because the investigations were performed on samples in different structures, growth methods and growth conditions, it is difficult to present a universal constant. In fact, there has been a relatively large variance in the values of bowing parameter reported so far.[4] Therefore in practical meaning, providing a simple and effective method seems more useful than trying to give a unified value of bowing parameter.

Reflectance measurement as a powerful method has been used in many works to yield the knowledge of optical constants and excitonic resonance structure of III-V column semiconductor materials.[6,7,8] The three characteristic excitons (A, B, and C) of the wurtize crystal structure GaN

and AlGaN are usually used to deduce the band gap energy (E_g). For GaN, the large exciton binding energy permits its excitons to exist even at room temperature. It is predictable that for $Al_xGa_{1-x}N$ also, the excitons will exist and strongly influence the room temperature band structure, specially in low Al composition region. On the other hand, reflectance measurement is, if possible, obviously convenient in determining the E_g of AlGaN alloys, compared with other optical spectroscopic methods, such as photoluminesence (PL), cathodoluminesence (CL), and optical absorption (OA) measurements. the recent study of Ochalski et al. has employed reflectance and photoreflectance (PR) spectra to determine the E_{FX} of AlGaN, but without any discussion on reflectance measurement.[9] More recently, Yu *et al.* have confirmed the feasibility of this measurement in estimating the E_g of AlGaN alloys in AlGaN/GaN heterostructures, but with a difference of 3% (above 100 meV) compared with PL measurement.[10] In the experiment, however, we found that the thickness variation of the AlGaN layer may change the line shape of reflectance spectrum and create uncertainty in determining the location of excitonic energy. It was shown that this uncertainty may be the reason for the large discrepancy between the reflectance and PL measurements. Hence the application of this method remains to be elucidated in model analysis and accuracy modification. For such purposes, a reflection model of two absorbing layers with a transparent substrate was used to perform a detailed discussion on the experimental data. Based on this discussion, the E_{FX}s of AlGaN obtained from a fitting procedure were found in an excellent agreement with that from PL measurement. Combining the results of the reflectance and XRD measurements, we obtained a downward bowing parameter b=0.53 eV in the excitonic transition band gap of AlGaN epilayer.

3.2 EXPERIMENTAL PROCEDURE

The samples in this study were grown on sapphire (0001) substrate by the horizontal atmospheric pressure metal-organic chemical-vapor deposition (MOCVD) method. Trimethygallium (TMGa),

Trimethyaluminium (TMAl), and ammonia (NH_3) were used as source materials for Ga, Al, and N. All the epitaxial layers were nominally undoped. The sapphire substrate was first heated at 1100℃ for 10 min. in a stream of hydrogen for cleaning. Then the temperature was lowered to 500℃ to grow a 30-nm GaN buffer layer. Subsequently, the temperature was elevated to 1080℃, at which a 1.5-μm-thick GaN layer and a AlGaN layer with a thickness between 30 and 200 nm was grown. The heterostructure is illustrated in Fig. 3.1. Reflection spectrum was measured in air for light normally incident to the surface of the sample with a 0.1 nm spectral resolution. A tungsten lamp was used as the light source. The peaks in reflectance spectra have also been confirmed by He-Cd laser source (325nm) PL measurement for low Al composition samples. XRD measurement was used a rotating anode Rigaku RINT2000 diffractometer, with Cu Ka_1/Ka_2 doublet (λ_{Ka1}=0.1540562 nm). The scan step was 0.002 degree. All measurements were carried out at room temperature.

3. 3 RESULTS AND DISCUSSION

3.3.1 Composition of the AlGaN layer

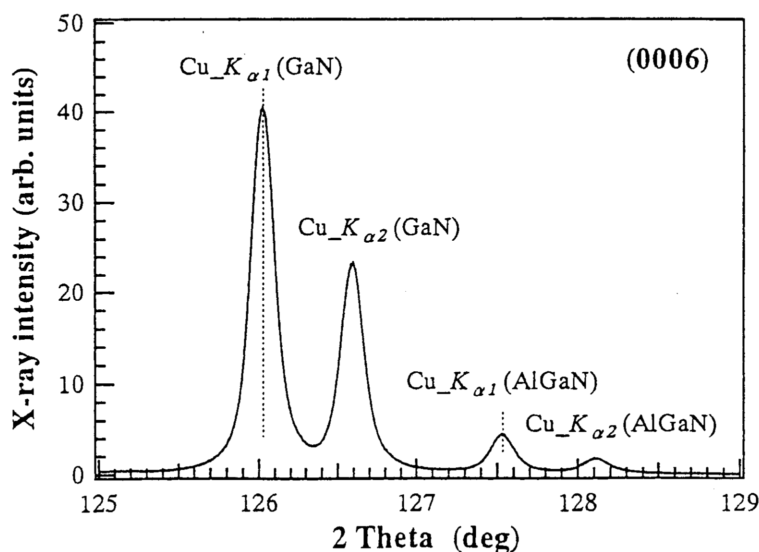

FIG. 3.1. XRD spectra for an $Al_xGa_{1-x}N$/GaN/Sapphire heterostructure.

For wurtzite structure $Al_xGa_{1-x}N$ crystal, the lattice parameter of principle crystal axis c can be

obtained from XRD measurement in the symmetric (0006) reflections of $2\theta/\theta$ mode by using the Bond method (Fig. 3.1, $c = \lambda_{K\alpha 1}/3\sin\theta = 0.1540562/3\sin\theta$ nm). The value for c is often used to calculate the mole fraction (x) assuming the validity of Vegard's law. Principally, the relaxed lattice parameters a_0 and c_0 from the binaries AlN and GaN, $a_0(x)$ and $c_0(x)$ of stress-free ternary $Al_x Ga_{1-x}N$ films should be related to mole fraction (x) by the linear expression

$$c_0(x) = c_0^{GaN}(1-x) + c_0^{AlN}x \ , \tag{3.1a}$$

$$a_0(x) = a_0^{GaN}(1-x) + a_0^{AlN}x \ . \tag{3.1b}$$

where the fully relaxed lattice constants, a_0 and c_0, are taken to be 3.1892 Å and 5.1850 Å for GaN,[11] and 3.1114 Å and 4.9792 Å for AlN,[12] respectively, values which are now widely accepted. However, in most cases, the lattice parameters are changed by lattice mismatch, thermal expansion change, point defects, and size effect, etc.[13] In view of these changes, the actual lattice parameters a and c could be, under a crucial assumption that in-plane biaxial strain is dominant in the AlGaN layer, related to the fully relaxed ones by strain ratio,

$$\varepsilon_c / \varepsilon_a = \frac{(c - c_0)}{c_0} / \frac{(a - a_0)}{a_0} = -2\frac{C_{13}}{C_{33}} \ . \tag{3.2}$$

where the C is the elastic stiffness constants of the AlGaN epitaxial layer. Considering that the elastic properties of ternary varies linearly with the composition of arbitrary binary compounds, AlN and GaN, the values C_{13}=114 and C_{33}=381 GPa ($\varepsilon_c / \varepsilon_a$ = -0.60) for GaN (Ref. 14) and C_{13}=120 and C_{33}=395 GPa ($\varepsilon_c / \varepsilon_a$ = -0.61) for AlN (Ref. 15) were used to set the value of strain ratio of AlGaN as -0.60 here, which is also identical to that used by Akasaki *et al.* in Ref. 16.

The mole fraction x of the alloys can then be calculated by solving Eqs. (3.1) and (3.2). Because the AlGaN films are so thin in this experiment and all samples show relative high 2DEG mobility, they can be considered as perfectly strained by GaN layers, and then we can assume that $a_0(x) = a_0^{GaN}$ here. The composition values therefore obtained from the measured lattice constants are shown in the next section.

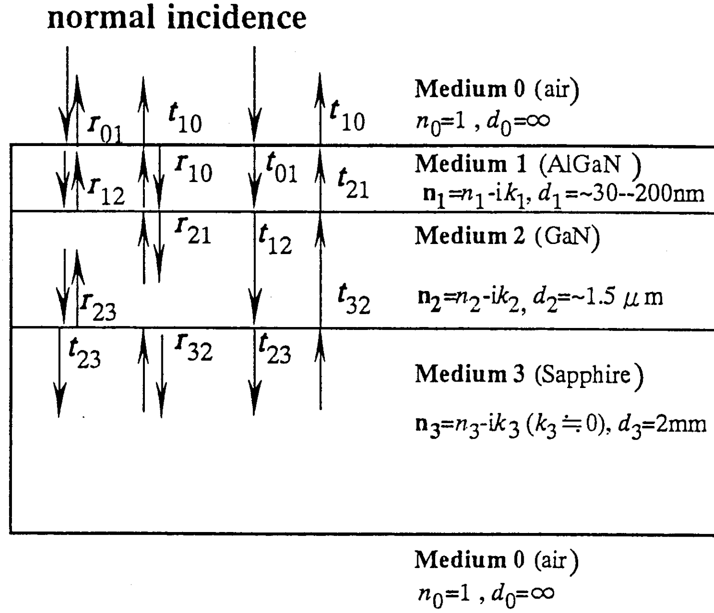

Fig. 3.2. Schematic diagram of the AlGaN/GaN/sapphire heterostructure and the reflection and transmission of the normal-incidence light in this multilayered system.

3.3.2 Interpretation of reflectance spectra

In Fig. 3.2, the AlGaN/GaN/sapphire multilayered structure is drawn schematically. Assuming that the thickness of sapphire substrate is infinite and the roughness of the top most epilayer is negligible, at normal incident, the power reflectance of this structure which takes the multiple reflection into consideration can be written as

$$R = |r|^2 = \left| r_{02} + \frac{t_{02}t_{20}r_{23}\exp(-2\alpha_2 d_2)\exp(-i\delta_2)}{1 - r_{23}r_{20}\exp(-2\alpha_2 d_2)\exp(-i\delta_2)} \right|^2 , \tag{3.3}$$

Where $$r_{02} = \frac{r_{01} + r_{12}\exp(-2\alpha_1 d_1)\exp(-j\delta_1)}{1 - r_{10}r_{12}\exp(-2\alpha_1 d_1)\exp(-j\delta_1)} , \tag{3.3a}$$

$$r_{20} = \frac{r_{21} + r_{10}\exp(-2\alpha_1 d_1)\exp(-j\delta_1)}{1 - r_{10}r_{12}\exp(-2\alpha_1 d_1)\exp(-j\delta_1)} , \tag{3.3b}$$

$$t_{02} = \frac{t_{01}t_{12}\exp(-\alpha_1 d_1)\exp(-j\delta_1 /2)}{1 - r_{10}r_{12}\exp(-2\alpha_1 d_1)\exp(-j\delta_1)} , \tag{3.3c}$$

$$t_{20} = \frac{t_{21}t_{10}\exp(-\alpha_1 d_1)\exp(-j\delta_1/2)}{1-r_{10}r_{12}\exp(-2\alpha_1 d_1)\exp(-j\delta_1)}, \tag{3.3d}$$

and

$$r_{ij} = \left|\frac{(n_i-n_j)^2+(\kappa_i-\kappa_j)^2}{(n_i+n_j)^2+(\kappa_i+\kappa_j)}\right|\exp(i\theta_{ij}) \text{ (ij=01, 12, 23; } r_{ij} = -r_{ji}\text{ , } \theta_{ij} = \arg(r_{ij})) \tag{3.4}$$

are, respectively, the Fresnel reflection coefficients of air/AlGaN, AlGaN/GaN and GaN/sapphire, and the corresponding transmission coefficient $t_{ij} = 1 + r_{ij}$. α is the absorption coefficient, n the refractive index, and d the thickness; $\delta_1 = \frac{4\pi}{\lambda}n_1 d_1$ and $\delta_2 = \frac{4\pi}{\lambda}n_2 d_2$; $\kappa_1 = \alpha_1\lambda/4\pi$ and $\kappa_2 = \alpha_2\lambda/4\pi$.

Using Eqs. (3.3), the reflectance spectra of AlGaN/GaN heterostructure was numerically calculated. In the calculation, the absorption coefficient spectrum of GaN was taken from our previous work; [17] the absorption spectrum of AlGaN was obtained from the rigid shift of GaN. For avoiding noticeable error, the Al mole fraction of AlGaN is set to be a relatively low value, $x \leqq 0.11$. The energy locations of the maxima of excitonic profiles in the absorption spectra of GaN and AlGaN, named E_{GM} and E_{AM} respectively, were used as identifications corresponding to the extrema in reflectance spectrum. Published data of Brunner *et al.* were used for the refractive index of GaN and $Al_{0.1}Ga_{0.9}N$ as a function of composition x and energy below the band gap.[18] Above the band gap, the data of Amano *et al.* were employed.[19]Sapphire is considered to be transparent with the refractive index as a function of wavelength quoted from Ref. 20. It should be mentioned that the phase factor $\exp(i\theta_{ij})$ in Eq. (3.4) may also contribute to the phase shift in reflectance spectrum. However, this is neglected in the most of the literature.

The details in the reflectance spectra can be explained by the calculated spectrum illustrated in Fig. 3.3. As expected, model calculations show that the excitonic structures in absorption spectra of GaN and AlGaN are just the cause of the corresponding valley and peak in the reflectance

spectrum. As shown in Fig. 3.3, the reflectance can be divided into three regions, which are the photon energy (a) below the absorption edge of GaN; (b) between the absorption edges of GaN and AlGaN; and (c) above the absorption edge of AlGaN.

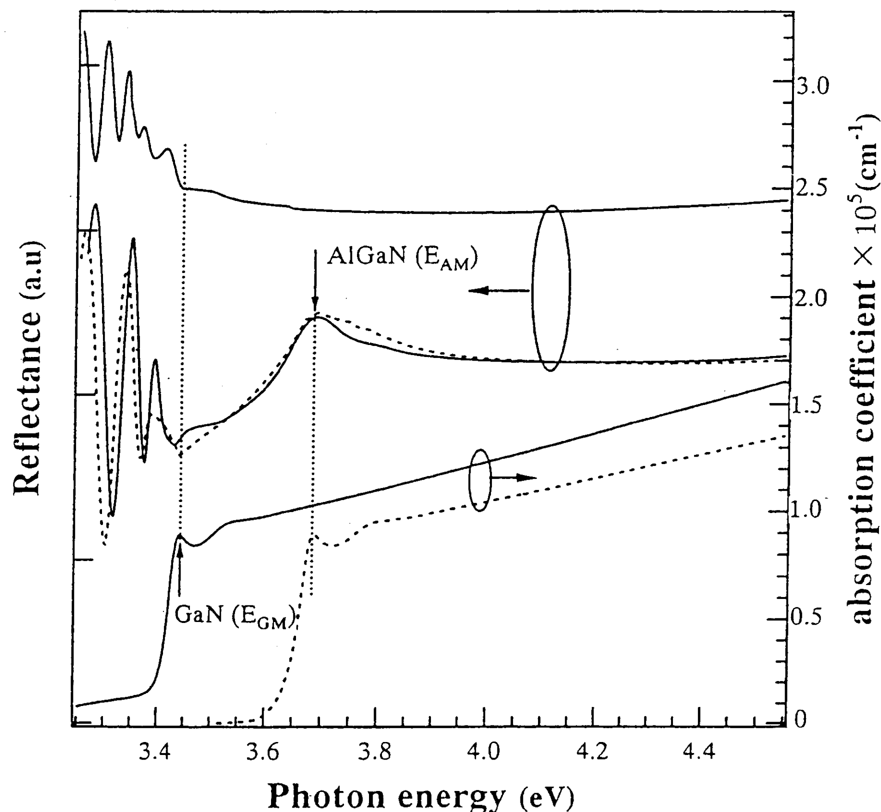

Fig. 3.3. Numerically calculated reflectance spectral of $Al_{0.11}Ga_{0.89}N$/GaN/sapphire heterostructure (dash line). The solid line represents the experimental data. Reflectance and absorption spectra of the GaN/sapphire structure are also given for comparison. E_{GM} and E_{AM} were used as identification responding to the maxima of exciton profiles in absorption spectra of GaN (solid line) and $Al_{0.11}Ga_{0.89}N$ (dashed line), respectively.

In the region (a), as the normal-incidence beam experiences relatively weak absorption, the reflected beam consists of the lights that reflected from the interfaces of air/AlGaN, AlGaN/GaN and GaN/sapphire. In this region, the reflectance spectrum is dominated by the interference effect results from both AlGaN and GaN layers phase factor $\exp(-j\delta_1)$ and $\exp(-j\delta_2)$. In the region (b), due to the strong absorption of the GaN layer, the second term in Eq. (3.3) tends to be negligible, and results in a drastically change in reflectance. Since the multiple reflections in the GaN layer were eliminated in this region, the reflected beam only comes from the lights reflected at

interfaces of air/AlGaN and AlGaN/GaN, and the shape of the reflectance spectrum is mainly dominated by the interference effect results from $\exp(-j\delta_1)$. As the energy of incident light further increases and reaches into region (c), the absorption of AlGaN rapidly increases, resulting in a sharp change in reflectance again.

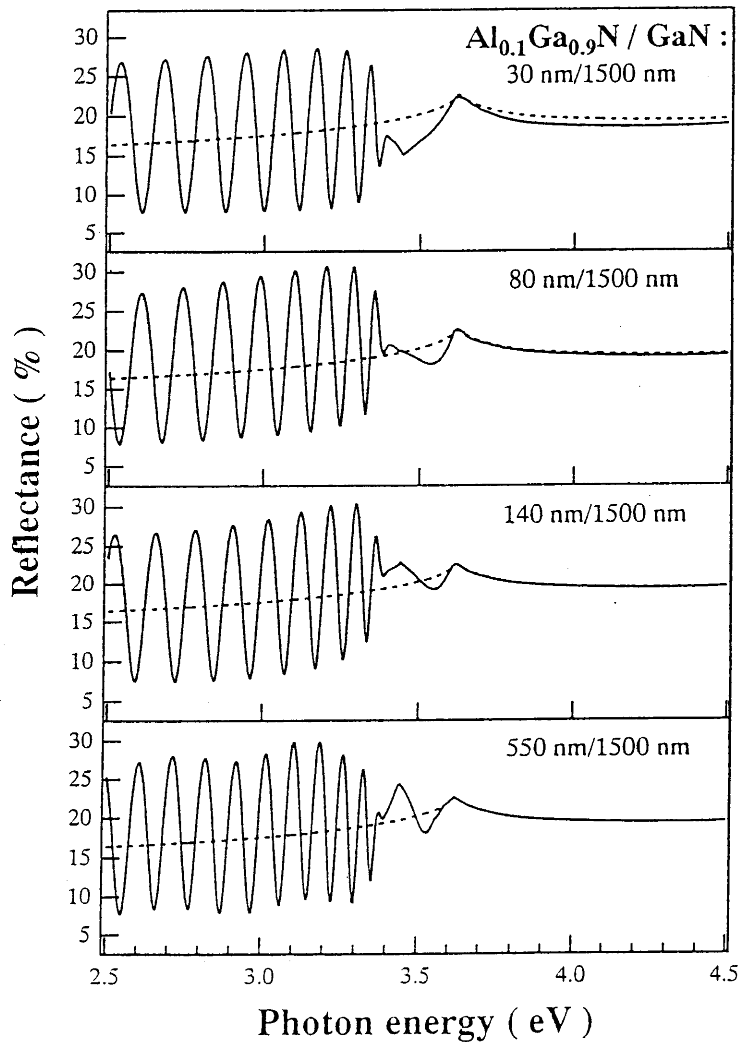

Fig. 3.4. Experimental reflectance spectra for $Al_xGa_{1-x}N$/GaN/Sapphire (x around 0.1) heterostructures with various thicknesses of AlGaN layers (d_1). The thickness values were measured by thickness monitor in the growth process of epilayers. It shows that the excitonic profile of GaN is hidden in interference fringes when d_1 is about 200 nm.

Besides the excitonic resonance structures of GaN and AlGaN, we would like to address the line shape of reflectance spectrum region (b), where the interference effect caused by the AlGaN layer may strongly modify the spectral line shape and confuse the recognition of the excitonic profile

desired. Figure 3.4 displays the experimental reflectance spectra of different thicknesses of AlGaN layers. For Al composition x around 0.1, we can see that the variation of d_1 results in noticeable changes in the spectral lineshapes of region (b). Specially, we found that when d_1 is about 200 nm [Figs. 3.4(c) and 3.4(d)], the reflectance spectra show quite a difference in shape. In Fig. 3.4(c), "two peaks" appear near the excitonic position of AlGaN and the excitonic profile of GaN seems to be hidden (3.403 eV seems to be an extremum value of interference fringes rather than a value of E_{GM} which is indicated by another arrow at about 3.43 eV); however, in Fig. 3.4(d) the excitonic peaks of GaN and AlGaN can be identified clearly. In order to be clear in assigning both AlGaN and GaN peaks from Figs. 3.4(c) and 3.4(d), the reflection model was again used to analyze the experimental spectra, where the thickness of the AlGaN layer is a variable parameter. Because heterostructure devices are usually grown on thick GaN, where thickness enables the multiple reflection in the GaN layer diminished at energy above E_g^{GaN}, the influence of the variation in thickness of the GaN layer (d_2) was not found and, therefore, was not concerned here.

In Fig. 3.5, the calculated spectra of different thicknesses of AlGaN layers are shown. As for the variation in thickness of the AlGaN layer (d_1), it was seen that the energy location E_{AM} of the identification line does not shift with the changes of thickness d_1, while the line shape changes just like the changes of the experimental one (Fig. 3.4). It was also found that the peak like shape presented below the E_{AM} [Fig. 3.5(c)] is a interference fringe result from the AlGaN layer when d_1 is 192 nm. Under the effect of this fringe, the excitonic profile of GaN is undistinguished, while that of AlGaN is still visible. For interpretation, we utilized the calculated spectra of R_{01} ($R_{01}=|r_{01}|^2$) as shown in Fig. 3.6. It comes as no surprise that the line shape of R_{01} exhibits a trend to agree with that of R as the thickness d_1 increases. We can know that in regions (b) and (c), the large value of $\alpha_2 d_2$ of the GaN layer lets $R \approx R_{02}$ [see Eq. (3.3)]. According to Eq. (3.3a), r_{02} will approach r_{01} as the d_1 increases, meaning that the thick enough d_1 will eliminate the multiple reflections in the AlGaN layer and only leave the reflected light of r_{01} remaining. As a result, R will approach to R_{01}. Figure 3.6 provides a direct observation that R_{01} acts as a dominant factor in the

amplitude of power reflectance R around the exciton resonance energies of AlGaN. Because R_{01} is not affected by the variation of thickness d_1, the excitonic profile of AlGaN cannot be diminished in the line shape changes. In contrast to the AlGaN layer, the GaN layer has to reflect its excitonic profile through the reflected lights of r_{12} and r_{23} and, therefore, it is easily affected by the interference effect and its excitonic profile may be hidden by the interference fringe. The calculated model demonstrates that the occurrence of interference fringe starts from about d_1=40 nm with a thickness period about 75 nm.

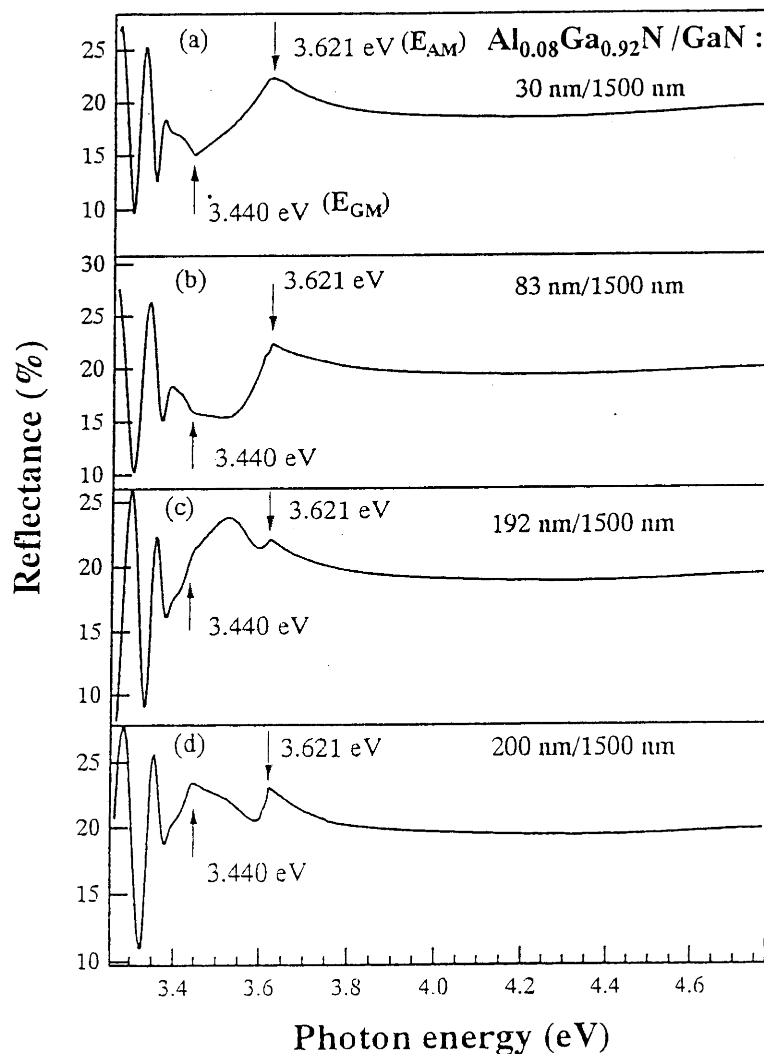

Fig. 3.5. Calculated reflectance spectra for $Al_{0.08}Ga_{0.92}N$/GaN/Sapphire heterostructures with thickness (d_1) changes corresponding to that in Fig. 3.4. The line shape of region (b) shows the changes in agreement with that in Fig. 3.4, while the energy location of E_{AM} (3.621 eV) are not shifted.

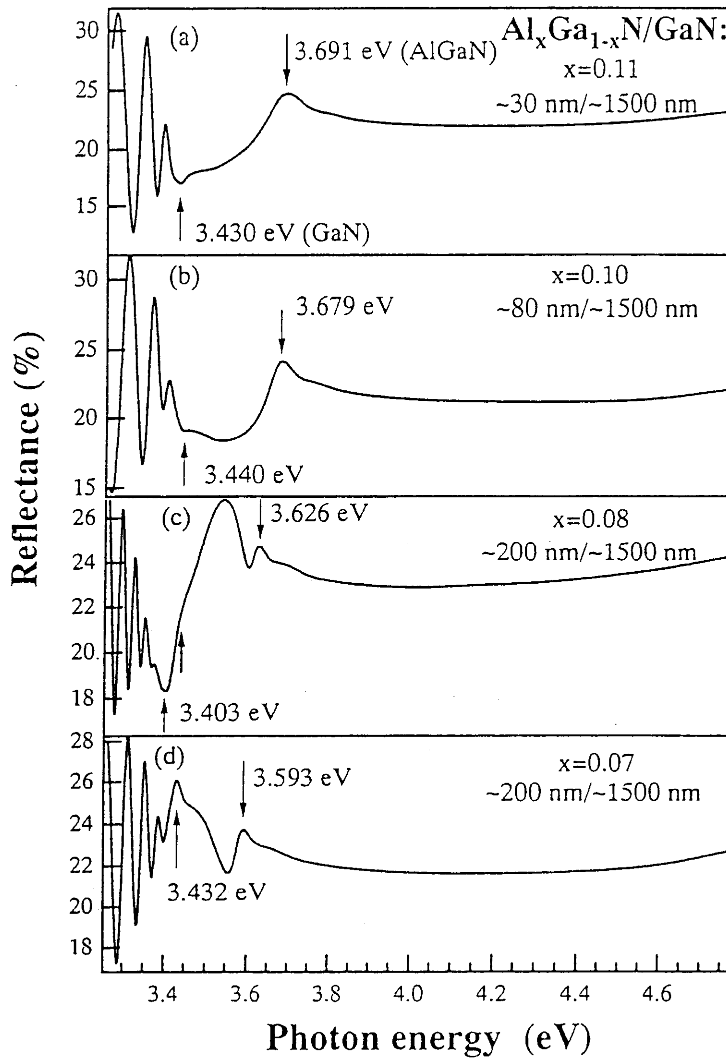

Fig. 3.6. Calculated reflectance spectra of R_{01} (dashed line) and R (solid line) with various thickness d_1. With the increase of d_1, R_{01} shows a trend of agreement with R at the excitonic profile of AlGaN. It also shows the amplitude of R_{01} is a dominant part in that of R.

We can summarize the results of the above analysis as: (i) without the presence of interference fringes [in region (b)], both excitonic profiles of GaN and AlGaN can be easily identified in the reflectance spectrum; (ii) with the presence of interference fringes, the excitonic profile of the GaN layer is possibly overlapped, but the excitonic profile of AlGaN can be observed. The interference fringes will only present at the low optical energy region of E_{FX} and not shift the excitonic position. This lets us easily assign the peak of AlGaN; (iii) the application of the reflectance measurement in AlGaN/GaN/sapphire heterostructures is not limited by the layer thickness of AlGaN (except AlGaN layer is too thin to be detected).

Figure 3.7 illustrates the experimental reflection spectra of AlGaN(~30nm)/GaN(~1500nm) samples with various Al mole fractions as a function of the photon energy. The positions around peak and valley of the spectra were taken as the free excitonic transition energies (E_{FX}) of the AlGaN and GaN layers, respectively, as indicated by arrows. Determination of the location of E_{FX} will be described in the next section.

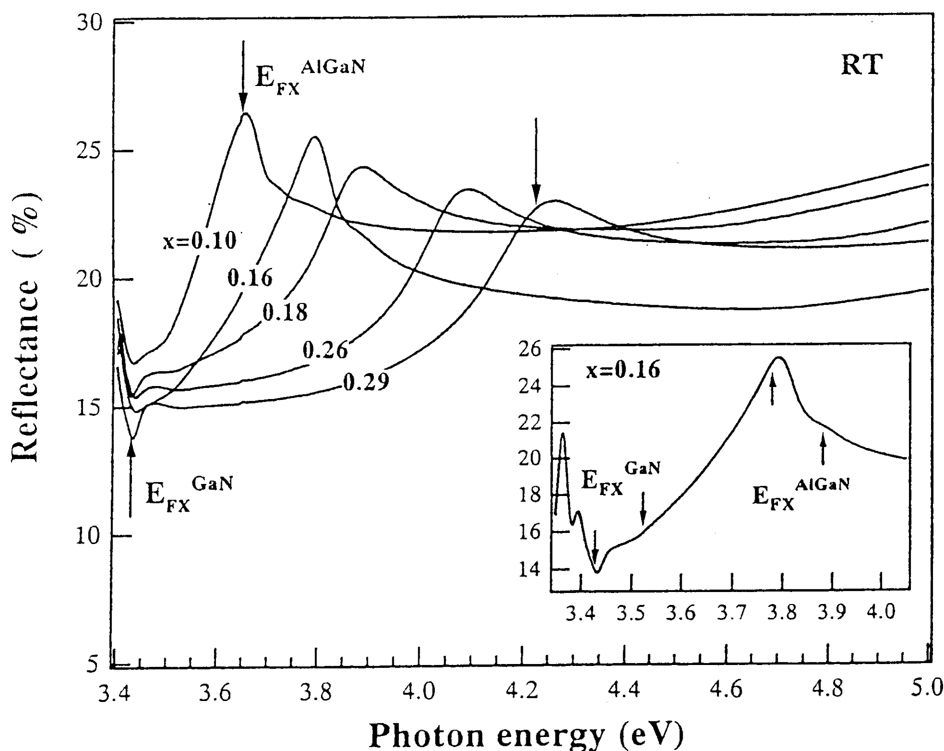

Fig. 3.7. Room temperature reflectance spectra of AlGaN(~30 nm)/GaN(~1500 nm) heterostructure samples with various Al mole fraction, x. The excitonic transition energies of GaN (E_{FX}^{GaN}) and AlGaN (E_{FX}^{AlGaN}) are marked by vertical arrows. The inset shows the spectrum of the x=0.16 sample. Broad features ascribed to exciton-LO phonon interaction were observed at optical energies about 100 meV above the E_{FX}^{GaN} and E_{FX}^{AlGaN}, respectively.

At room temperature, the three characteristic excitons (A, B, and C) could not be individually observed and were arranged in one broadened valley. We can see that with the increase of Al composition x, the E_{FX} of AlGaN shows a clear shift to the high energy left. Another interest is that, for the samples of $x \leqq 0.16$, the reflectance spectrum exhibits broad features at which the energy is about 100 meV above the free excitonic transition energies of GaN and AlGaN,

respectively. Similar features have been reported by several studies in the absorption spectra of GaN epilayers taken at low[21] and room temperature[22]. However, to the best of our knowledge, there have been no reports on the observation of such features in neither absorption nor reflectance spectra of AlGaN alloys. It was suggested that this broad structure is due to the exciton-LO phonon interaction in an indirect phonon-assisted absorption process which an incident photon simultaneously generates a ground state free exciton and a LO phonon, resulting in a resonance feature at the corresponding energy in the spectrum. In the range of $0 \leqq x \leqq 0.15$, the LO-phonon energy of $Al_xGa_{1-x}N$ ranges from about 735 cm^{-1} (91.2 meV) to 770 cm^{-1} (95.5 meV).[23] By reason of the exciton dispersion, the energy spacing between the maximum of broad feature and the band edge exciton is slightly higher than one LO-phonon energy.[22] The observed features indicate that LO phonon assisted exciton formation also plays an efficient part in the $Al_xGa_{1-x}N$ alloys (in this case, $x \leqq 0.16$). For Al mole fraction above 0.16, the exciton-LO phonon interaction were no longer visible (Fig. 3.7) and may be attributed to the alloy broadening effect, due to the increase of Al content, which leads to a decrease of the Bohr radius of the free exciton in AlGaN[24] and makes the broad feature merge into the broaden excitonic profiles.

3.3.3 Free exciton transition energy and bowing parameter

In the spectral region which is of excitonic profile, we can determine the energy locations of the excitons with a simplified procedure. The spectral lineshape due to the exciton transition of energy $h\nu_i$ can be approximately described in a form of Lorentzian dispersion,

$$R(\nu) = R_0 + A_i \operatorname{Re}\left[\frac{h\nu_i - h\nu + i\Gamma_i}{(h\nu - h\nu_i)^2 + \Gamma_i^2}\exp(i\Theta_i)\right], \tag{3.5}$$

where R_0 is a constant of background reflectance, and A_i, $h\nu_i$, Γ_i, and Θ_i denote, respectively, the amplitude, the energy location, the broadening parameter and the phase factor of exciton i (i=A, B, C). [25]

At room temperature, the three discrete excitons (A, B, and C) could not be individually distinguished. However, they still have a strong impact upon the reflectance spectra that nonexcitonic models cannot fit.[26] In order to perform meaningful fits to the spectra, the minimum possible number of free parameters were tried. In case of normal incidence, namely, E⊥c axis, the resonance strength of the exciton C band to conduction band transition ($\Gamma_{lv}^{7} \rightarrow \Gamma_{c}^{7}$) is very weak in the resonance strength.[27] Therefore the exciton resonance structures in the reflectance spectra are dominated by the A and B exciton transitions here. Considering that the A and B excitons are relatively close in energy, we treated the A_i, Γ_i, and Θ_i of two excitons as the same one in the fitting process.

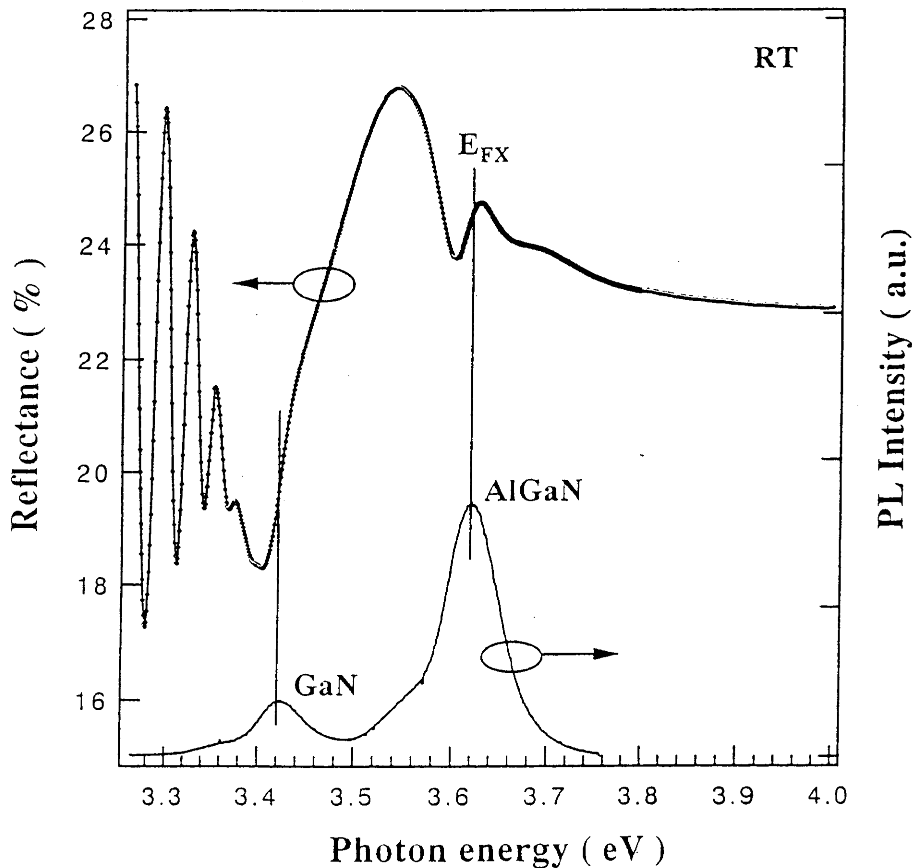

Fig. 3.8. A typical fitting curve of the experimental reflectance spectrum of $Al_{0.08}Ga_{0.92}N$/GaN heterostructure with the AlGaN layer about 200 nm. The free exciton transition energy (E_{FX}^{A}) obtained shows a good agreement with the peak energy of the PL spectrum.

For the purpose of comparison, we also performed room temperature PL measurements on the

samples of $x<0.16$ AlGaN alloys, where the exciton resonance energies are below the excitation energy of the 325 nm He-Cd laser source (3.815 eV). A typical comparison of reflectance and PL spectra is shown in Fig. 3.8. The free exciton transition energy of A ($\Gamma_v^9 \rightarrow \Gamma_c^7$, E_{FX}^A) is obtained by least-squares fit of Eq. (3.5) in reflectance spectrum. Table 3.1 summarizes the results of two measurements, and shows that the difference in E_{FX}^A of AlGaN is less than 6 meV. Such a result is acceptable because numerous studies have demonstrated the fact that for undoped GaN and its ternary compound AlGaN, the dominant peak in room temperature PL spectrum is due to the free exciton transition (FX).[28]

Table 3.1. Comparison of the free exciton transition energies (E_{FX}^A) of $Al_xGa_{1-x}N$ ($x<0.16$) epilayers determined from the reflectance spectra and the peak energies obtained from PL measurements.

Sample	No.1	No.2	No.3	No.4	No.5	No.6	No.7
PL E_g (eV)	3.533	3.578	3.600	3.621	3.667	3.669	3.695
Reflec. E_g (eV)	3.527	3.583	3.606	3.621	3.664	3.667	3.700

Strictly speaking, the band gap energy is defined as the sum of free exciton transition energy (E_{FX}) and its binding energy (E_b), namely $E_g=E_{ex}+E_b$. However, the condition is complicated in ternary compound AlGaN. Up to now the binding energy of AlN is not clear. Moreover, no precise knowledge is available on the composition dependence of effective masses in $Al_xGa_{1-x}N$ ternary alloys so far. In practicality, the transition energy of free exciton can be treated as one of the most precise substitutes of true band gap energy (E_g), namely, the excitonic bandgap.[29]

The nonlinear dependence of the lowest direct band gap energy on the Al mole fraction can be written in the follow expression,

$$E_g^{AlGaN} = E_g^{GaN}(1-x) + E_g^{AlN}x - bx(1-x), \tag{3.6}$$

where E_g (GaN) and E_g (AlN) are the room temperature band gap energies determined to be 3.43 eV and 6.20 eV for our samples.

The group values of x and E_g of AlGaN alloys were hence used to determine bowing parameter (b) by fitting Eq. (3.6). In Fig. 3.9, the fitting plot shows a value of b=0.53 eV, close to the

reported value of 0.69 eV in Ref. 4 and 0.60 eV in Ref. 29. It is interesting to note that the samples used in Refs. 4 and 29 were close to the samples used here in structures. In addition, analysis of the measured c lattice parameter shows that the AlGaN layers in all of the heterostructures were subjected to an in-plane tensile biaxial strain. It is known that the band gap, under the tensile strain, decreases relative to the unstained result. This in turn supports that the bowing in the AlGaN band gap is downward.

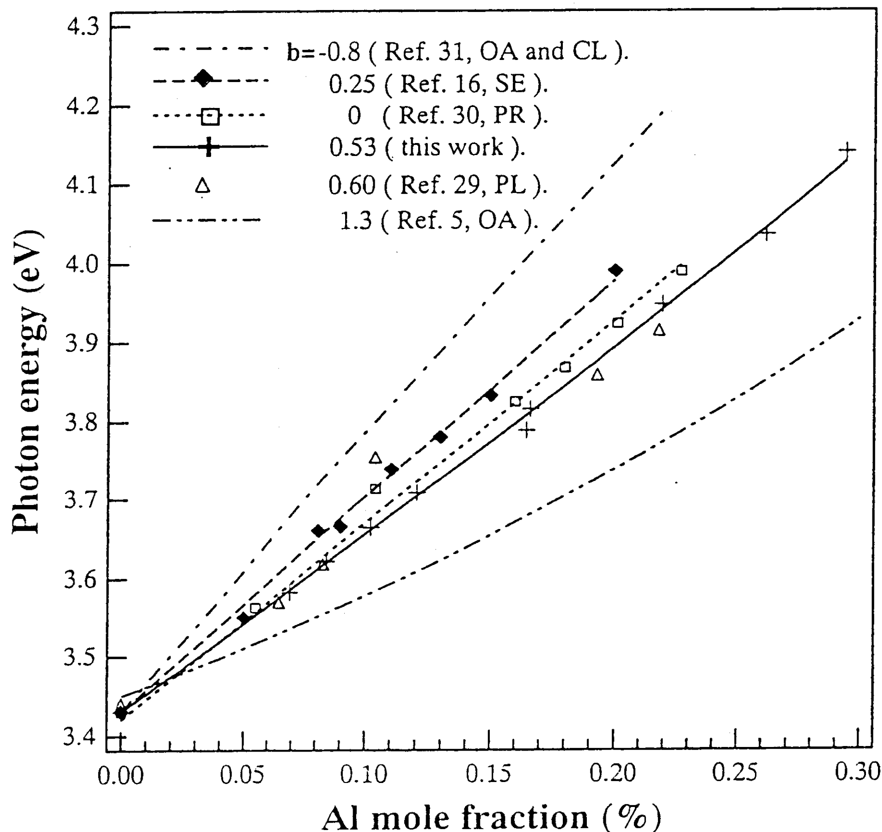

Fig. 3.9. Al composition dependence of the exciton transition energies derived from the reflectance measurement. Such dependencies of band gap energy derived from CL, OA, PL, PR, and spectroscopic ellipsometry (SE) methods in literature were shown together.

3.4 SUMMARY

In summary, a simple method combining the normal incident reflectance with XRD measurement to determine the Al mole fraction and bowing parameter of AlGaN alloys was presented. By using

a reflection model of two absorbing layers with a transparent substrate, the power reflectance of AlGaN/GaN/sapphire heterostructure was numerically calculated. The results of the model calculations show a good agreement with that of the experiments. Based on these calculations, a discussion concerning the confirmation of excitonic profile and the influence from the thickness variation of AlGaN layer was performed. Analysis shows that the reflectance measurement is indeed feasible in determining the free exciton transition energy (E_{FX}) of AlGaN epilayer in AlGaN/GaN heterostructure.

A precise value of E_{FX} was obtained by performing theoretical fit on the excitonic profile of a AlGaN epilayer. Comparing with He-Cd laser source PL measurement, it was found that the difference between the E_{FX}^{A} and the corresponding peak energy is less than 6 meV. In the low Al composition ($x \leqq 0.16$), the reflectance spectral features of exciton-LO phonon interaction were observed at an optical energy ~100 meV above the transition energy of band edge exciton of AlGaN. This observation indicates that the samples under investigation are of high quality and also provides support that the energy locations of E_{FX}^{A} identified are correct. With consideration of in-plane biaxial strain, Al mole fractions were determined by using both lattice parameters of a and c obtained from XRD measurement by using the Bond method. In the composition range of $0 \leq x < 0.3$, we found a downward bowing in the band gap of AlGaN epilayer with a bowing parameter of b=0.53.

References

[1] M. A. Khan, A. Bhattarai, J. N. Kuznia, and D. T. Olson, Appl. Phys.Lett. **63**, 1214 (1993); M. A. Khan, M. S. Shur, J. N. Kuznia, Q. Chen, J. Burn, and W. Schaff, Appl. Phys. Lett. **66**,1083 (1995); S. N. Mohammad, Z. F. Fan, A. Salvador, O. Aktas, A. E. Botchkarev, W. Keim, and H. Morkoc, Appl. Phys. Lett. **69**,1420 (1996); Q. Chen, M. A. Khan, J. W. Yang, C. J. Sun, M. S. Shur, and H. Park, Appl. Phys. Lett. **69**,794 (1996).

[2] S. Itoh *et al.*, Jpn. J. Appl. Phys. **32**, L1530 (1993); R. L. Aggarwal, P. A. Maki, R. J. Molnar, Z. L. Liau, and I. Melngailis , J. Appl. Phys. **79**, 2148 (1996).

[3] G. Y. Xu, A. Salvador, W. Kim, Z. Fan, C. Lu, H. Tang, H. Morkoc, G. Smith, M. Estes, B. Goldenberg, W. Yang, and S. Krishnankutty, Appl. Phys. Lett. **71**, 2154 (1997).

[4] S. R. Lee, A. F. Wright, M. H. Crawford, G. A. Petersen, J. Han, and R . M. Biefeld, Appl. Phys. Lett. **74**, 3344 (1999), and references therein.

[5] H. Angerer, D. Brunner, F. Freudenberg, O. Ambacher, M. Stutzmann, R. Hopler, T. Metzger, E. Born, G. Dollinger, A. Bergmaier, S. Karsch, and H.-J. Korner, Appl. Phys. Lett. 71, 1504 (1997).

[6] H. Ehrenreich, H.R. Philipp, and J. C. Phillips, Phys. Rev. Letters **8**, 59 (1962); H.R. Philipp and H. Ehrenreich, Phys. Rev. **129**, 1550 (1963).

[7] D. D. Sell, Phys. Rev. **B 6**, 3750 (1972); D. D. Sell, H. C. Casey Jr., and K. W. Wecht, J. Appl. Phys. **45**, 2650 (1974).

[8] W. Shan, B. D. Little, A. J. Fischer, J. J. Song, B. Goldenberg, W. G. Perry, M. D. Bremser, and R. F. Davis, Phys. Rev. **B 54**, 16 369 (1996); R. Stepniewski, K. P. Korona, A. Wysmolek, J. M. Baranowski, K. Pakula, M. Potemski, G. Martinez, I. Grzegory, and S. Porowski, Phys. Rev. **B 56**, 15 151 (1997);

[9] T. J. Ochalski, B. Gil, P. Lefebvre, N. Grandjean, J. Massies, M. Leroux, Solid State Commun. **109**, 567 (1999); T. J. Ochalski, B. Gil, P. Lefebvre, N. Grandjean, J. Massies, M.

Leroux, S. Nakamura, and H. Morkoc, Appl. Phys. Lett. **75**, 1419 (1999).

[10] L. S. Yu, D. Qiao, S. S. Lau, and J. N. Redwing, Appl. Phys. Lett. **75**, 1419 (1999).

[11] T. Detchprohm, K. Hiramatsu, K. Itoh, and I. Akasaki, Jpn. J. Appl. Phys., Part 2 **31**, L1454 (1992).

[12] F. A. Ponce, J.S. Major,Jr., W. E. Plano, and D. F. Welch, Appl. Phys. Lett. **65**, 2302 (1994).

[13] M. Leszczynski, H. Teisseyre, T. Suski, I. Grzegory, M. Bockowski, J. Jun, S. Porowski, K. Pakula, J. M. Baranowski, C. T. Foxon, and T. S. Cheng, Appl. Phys. Lett. **69**, 73 (1996).

[14] M. Yamaguchi, T. Yagi, T. Azuhata, T. Sota, K. Suzuki, S. Chichibu, and S. Nakamura, J. Phys.: Condens. Matter **9**, 241 (1997).

[15] K. Tsubouchi and N. Mikoshiba, IEEE Trans. Sonics Ultrason. **SU-32**, 634 (1985).

[16] I.Akasaki and H. Amano, Jpn. J. Appl. Phys., Part 1 **36**, 5393 (1997).

[17] G. Y. Zhao, H. Ishikawa, H. Jiang, T. Egawa, T. Jimbo, and M. Umeno, Jpn. J. Appl. Phys., Part 2 **38**, L993 (1999).

[18] D. Brunner, H. Angerer, E. Bustarret, F. Freudenberg, R. Hopler, R. Dimitrov, O. Ambacher, and M. Stutzmann, J. Appl. Phys. **82**, 5090 (1997).

[19] H. Amano, N. Watanabe, N. Koide, and I. Akasaki, Jpn. J. Appl. Phys., Part 2 **32**, L1000 (1993).

[20] Handbook of Optical Constants of Solids II, edited by E. D. Palik (Academic, New York, 1991).

[21] J. F. Muth, J. H. Lee, I. K. Shmagin, R. M. Kolbas, H. C. Casey, Jr., B. P. Keller, U. K. Mishra, and S. P. DenBaars, Appl. Phys. Lett. **71**, 2572 (1997).

[22] W. Shan, A. J. Fischer, S. J. Hwang, B. D. Little, R. J. Hauenstein, X. C. Xie, J. J. Song, D. S. Kim, B. Goldenberg, R. Horning, S. Krishnankutty, W. G. Perry, M. D. Bremser, and R. F. Davis, J. Appl. Phys. **83**, 455 (1998).

[23] D. Behr, R. Niebuhr, J. Wagner, K.-H. Bachem, and U. Kaufmann, Appl. Phys. Lett. **70**,

363 (1997).

[24] G. Steude, B. K. Meyer, A. Goldenr, A. Hoffmann. F. Bertram, J. Christen, H. Amano, and I. Akasaki, Appl. Phys. Lett. **74**, 2456 (1999).

[25] K. P. Korona, A. Wysmoelk, K. Pakula, R. Stepniewski, J. M. Baranowski, I. Grzegory, B. Lucznik, M. Wrblewski, and S. Porowski, Appl. Phys. Lett. **69**, 788 (1996).

[26] J. F. Muth, J. D. Brown, M. A. L. Johnson, Z. H. Yu, R. M. Kolbas, J. W. Cook, Jr. and J. F. Schetzina, MRS Internet J. Nitride Semicond. Res. **4S1**, G5.2 (1999).

[27] R. Dingle, D. D.Sell, S. E. Stokowski, P. J. Dean, and R. B. Zetterstrom, Phys. Rev. **B 3**, 497 (1971).

[28] G. Steude, D. M. Hofmann, B. K. Meyer, H. Amano, and I. Akasaki, Phys. Status Solidi A **165**, R3 (1998); B. Monemar, J. P. Bergman, I. A. Buyanova, W. Li, H. Amano, and I. Akasaki, MRS Internet J. Nitride Semicond. Res. **1**, 2 (1996); S. Chichibu, T. Azuhata, T. Sota, and S. Nakamura, J. Appl. Phys. 79(5), 2784 (1996).

[29] G. Steude, D. M. Hofmann, B. K. Meyer, H. Amano, and I. Akasaki, Phys. Status Solidi B **205**, R7 (1998).

[30] T. J. Ochalski, B. Gil, P. Lefebvre, N. Grandjean, M. Leroux, J. Massies, S. Nakamura, and H. Morkoc, Appl. Phys. Lett. **74**, 3353 (1996).

[31] S. Yoshida, S. Misawa, and S. Gonda, J. Appl. Phys. **53**, 6844 (1982).

CHAPTER 4
Back-Illuminated GaN MSM Structure UV Photodiode

4.1 INTRODUCTION

Ultraviolet (UV) photodetectors (PDs) have a wide range of commercial applications, such as flame sensors, engine monitoring, UV calibration devices and secure intersatellite/underwater communications. Due to their direct and wide band gap, GaN-based compounds are the ideal choice for the fabrication of various UV detectors. Among the different types of UV photodetectors, the metal-semiconductor-metal (MSM) photodiode is a promising candidate owing to its ease of fabrication and monolithical integration with field-effect transistor (FET)-based preamplifiers. Recently, several high-performance Schottky MSM-PDs based on GaN and AlGaN materials have been demonstrated;[1,2,3] however, they still suffer from performance limitations which impede their development toward practical applications. A well-known drawback of the MSM-PDs is the relatively low responsivity due to the shadowing of the active area by the electrodes and the consequent loss of efficiency. Semitransparent electrode may be used to improve the quantum efficiency, however, the main problem is their ability to reject the visible and near UV which may be affected by the internal photoemission at the metal/GaN interface, giving some response from the active region gap energy down to the Schottky barrier height. Although this problem has been overcome in GaAs based Schottky MSM-PDs by back illumination,[4,5] there has been no comparable report on devices of the same structure based on GaN. Since sapphire substrate is transparent in the wavelength range of interest, back illumination can be readily used to improve the sensitivity of GaN/sapphire material-structure MSM-PDs by avoiding electrode shadowing. In this study, back- illuminated GaN MSM-PDs with a thin active layer of 0.3 μm were thus fabricated and characterized. Compared with its top-illuminated counterpart, the back-illuminated MSM-PD exhibits a marked enhancement in responsivity with a value of 16.5

A/W at an applied bias of 5 V under irradiance of 5 μW/cm^2.

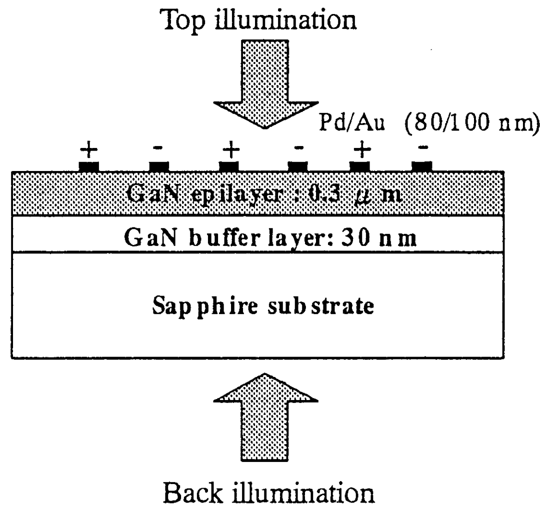

Fig. 4.1. A schematic cross section of the structure of the GaN MSM-PD.

4.2 EXPERIMENTAL PROCEDURES

The cross-sectional structure of MSM-PDs fabricated in this work is illustrated in Fig. 4.1. Double-polished sapphire substrates were used for back surface illumination. An epitaxial layer of GaN was grown on (0001) sapphire by the horizontal atmospheric pressure metal-organic chemical-vapor deposition (MOCVD) method. TMG and NH_3 were used as material sources, and H_2 was used as the carrier gas. Before the film growth, the substrate was heated at 1180℃ in a stream of hydrogen for 10 min. A low-temperature GaN buffer layer (30 nm) was deposited at 500 ℃ immediately before the growth of unintentionally doped epitaxial GaN (0.3 μm) at 1130℃. Room-temperature Hall effect measurement revealed that the background carrier concentration is 5.6×10^{16} cm^{-3}. Figure 4.2 illustrates the transmission spectrum of the grown sample and the deduced spectral absorption coefficient of the GaN epilayer. A clear absorption peak due to free excitons at 360 nm and Fabry-Perot oscillation with a high transmittance of 0.81 at 385 nm demonstrates that the GaN epilayer is of high crystalline and optical quality.

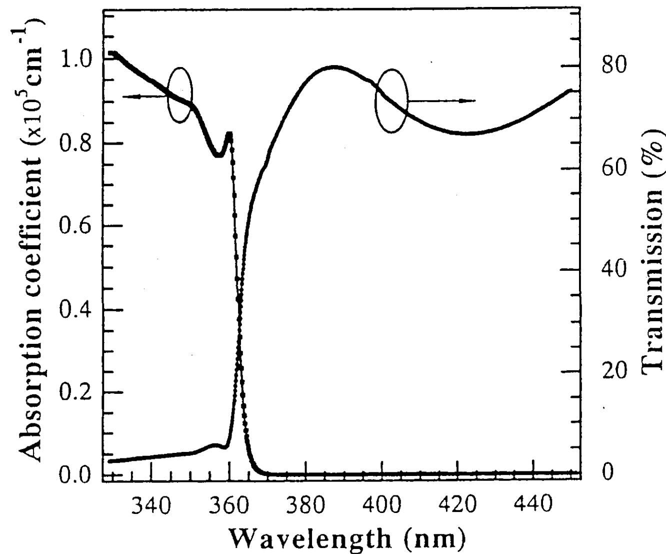

Fig. 4.2. Trasmission spectrum of the wafer with normal-incident light from the back surface and the deduced absorption spectrum of the GaN epilayer.

For the MSM structure, interdigitated patterns with the active area of $100 \times 105\ \mu m^2$, finger width of 5 μm, and gap spacing of 15 μm were defined by photolithography using a Hg-Xe lamp source (see Fig. 4.3). The Schottky contacts of Pd/Au (80/100 nm) were deposited by electron-beam evaporation and formed by a standard lift-off process. Prior to the vacuum deposition, the wafers were cleaned with organic solvents and then dipped in boiling aqua regia (HNO_3:HCl=1:3) solution for 15 min to remove the possible surface oxide of GaN followed by de-ionized water rinse. At last, the samples were annealed in a flowing nitrogen atmosphere at 300 ℃ for 20 min, to improve the Schottky barrier height and ideal factor.[6,7]

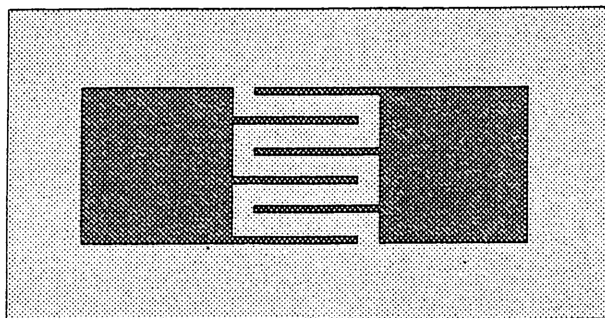

Fig. 4.3. Top view of MSM-PD showing the interdigitated geometry (finger width of 5 μm, and gap spacing of 15 μm

4.3 PERFORMANCE-CHARACTERISTICS ANALYSIS

4.3.1 Dark Current-Voltage Characteristics

The dark current is a very important parameter for characterizing the reliability and detecting ability of MSM-PDs. A low dark current may effectively diminish the current noise and then lower the minimum detectable power. In this work, a HP4145B semiconductor parameter analyzer with an accuracy limitation of 10 fA was used to record the current- voltage (I-V) characteristics of the MSM-PDs.

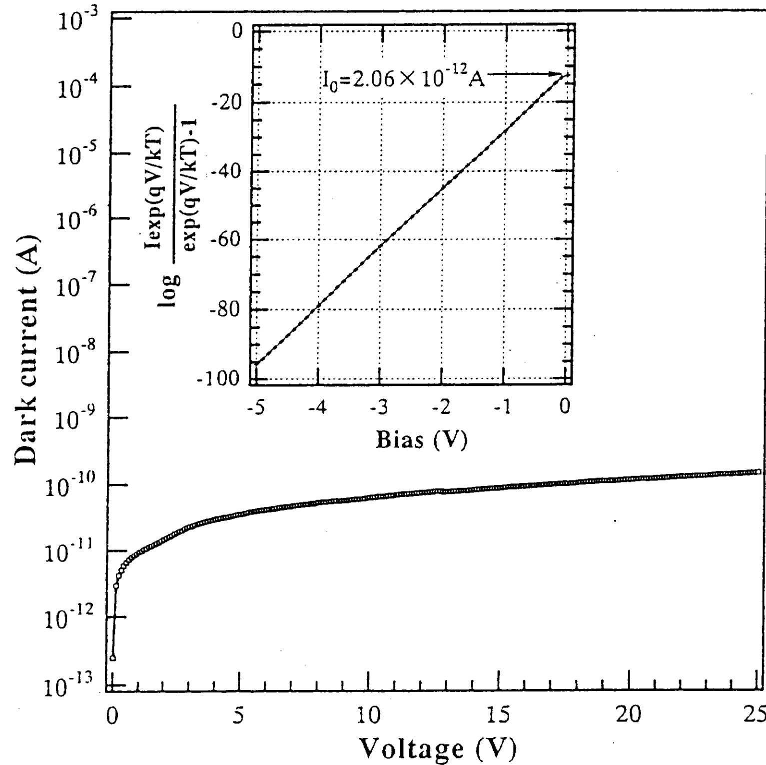

Fig. 4.4. Dark current I-V characteristics for MSM-PD. The inset is a logarithmic plot of $I\exp(qV/kT)/[\exp(qV/kT)-1]$ vs V.

As can be seen in Fig. 4.4, a low dark current was achieved at room temperature. The value of the current is 36 pA for a typical sample at 5 V bias. It was also found that no degradation occurred up to 70~80 V, demonstrating good dark *I-V* characteristics. Considering the MSM structure, consisting of two Schottky contacts connected back to back, the dark current of the detector can be described as[8]

$$I_{dark} = I_0 \exp(qV/nkT)[1-\exp(-qV/kT)],$$

$$I_0 = AA^{**}T^2 \exp(-q\phi_B/kT), \tag{4.1}$$

where V is the applied bias, A is the contact area and the other symbols have their conventional meanings. A logarithmic plot of $[I\exp(qV/kT)]/[\exp(qV/kT)-1]$ vs V was shown in the inset of Fig. 4.3. From the slope of this straight line, the ideal factor was determined to be n=1.01. The value of n is close to unity, indicating that the surface states are negligible. The intercept of this line shows that the saturation current is $I_0=2.06\times10^{-12}$ A, and the corresponding current density is $J_0=1.72\times10^{-6}$ A/cm^2. Using the value of the effective Richardson constant of A^*= 26.4 cm^{-2}K^{-2},[9] we obtained the effective Schottky barrier height ϕ_B=0.83 eV for the employed metallization scheme of Pd/Au.

4.3.2 Responsivity

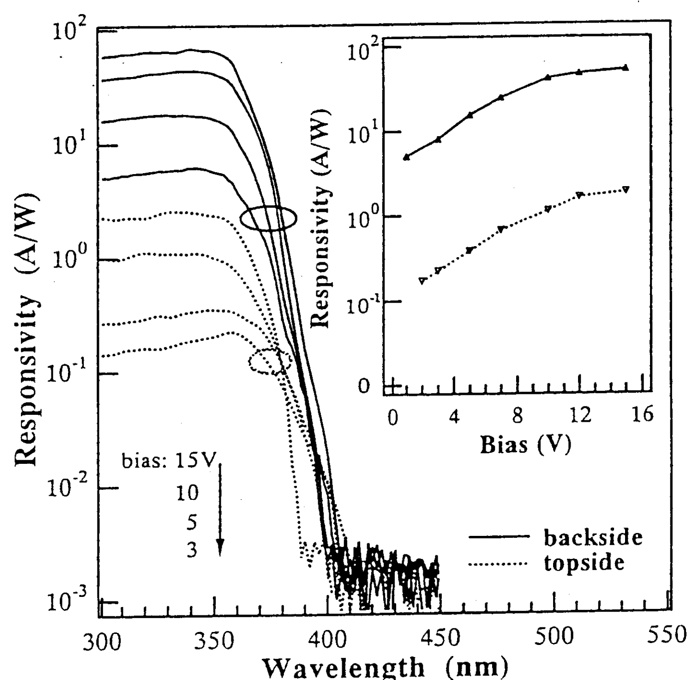

Fig. 4.5. Top- and back-illuminated spectral response of GaN MSM-PD biased at 15, 10, 5, 3 V. The inset shows the bias dependence of responsivity for the two illumination conditions.

Figure 4.5 depicts the top- and back-illuminated spectral responses of MSM-PD biased at 15, 10, 5 and 3 V. A UV-visible spectrophotometer with a xenon-arc lamp source and a monochromator with a grating of 600 lines/mm was used for these measurements in the range of 450~300 nm. The absolute values of responsivity were determined using a calibrated Si detector. For all spectra, there is a visible-radiation rejection of three to four orders of magnitude at the absorption edge under the constant irradiance density of 5 μW/cm^2. For both the top and back

illumination conditions, the responsivities remain reasonably flat for photons with energies above the band gap. In the optical energy range above the band gap, responsivity larger than 0.3 A/W was obtained for top illumination at a typical reverse bias of 5 V, which is in good agreement with the report.[1] A marked enhancement in responsivity was found under the back-illumination condition with a value of 16.5 A/W at 350 nm for the same bias. Since the responsivity of the back-illumination condition is about 55 times that of the top-illumination condition, the increase of responsivity cannot be ascribed only to the avoidance of the shadowing of electrodes. It was found that the responsivities show a linear dependence on bias voltage (inset of Fig. 4.5). Such behavior indicates the presence of internal gain in the devices. That is, the real current responsivity of an MSM-PD at photon energy $h\nu$ should be expressed as:

$$R_i = \frac{\eta_{ext} q}{h\nu} \cdot \Gamma_G, \tag{4.2}$$

where η_{ext} is the external quantum efficiency, q the electronic charge, h Planck's constant, ν the frequency of light, and Γ_G the internal gain. For top- and back-illumination conditions, the measured spectral responsivities yield $\eta_{ext}\Gamma_G$ products of 1.1 and 56.8, respectively, at 5 V bias, which evinces the existence of high internal gain in the case of back illumination.

4.3.3 Internal Gain

Internal gain has been found in both GaN- and GaAs-based Schottky MSM-PDs.[1-3,10,11] Most likely, the mechanism responsible for the internal gain is the increased electron injection at the cathode contacts due to the lowering of the barrier height by photoinduced hole accumulation.[12,13] The accumulation of holes may result either from the trapping of holes close to the cathode or the different transit speeds between the electrons and holes, where electrons traveling faster than holes leave a residual density of holes at the cathodes. Another effect of hole accumulation is field reduction in the gap region of the metal finger due to charge screening, resulting in an increased recombination probability for electron-hole pairs, i.e., resulting in a linear responsivity dependence on voltage.

A recent study on GaN-based Schottky barrier photodiodes and MSM-PDs by Katz *et al.* revealed that the surface states at the semiconductor-metal interface can trap photogenerated holes, thus reducing the Schottky barrier height and producing gain in the UV photoresponse.[14] In order to explain the internal gain, they invoke the existence of trapping states at the GaN surface at concentration, N_{ss} , of ~5×10^{9} cm^{-2} as reported in the literatures.[15,16] These traps are attributed to threading edge dislocations, having acceptor-like nature, with midgap energy. Positioned below the Fermi level, these traps are negatively charged. Photogenerated holes generated at the depletion region, drift towards the metal–semiconductor interface due to band bending. The holes are then trapped at the surface sites, and produce net positive charge $Q_{ss}=qN_{ss}$. The metal negative charge Q_{m}, and the positive depletion charge Q_{d} due to uncompensated donors, must satisfy the junction neutrality condition

$$Q_{m}+Q_{d}+Q_{ss}=0. \qquad (4.3)$$

Therefore, the depletion charge Q_{d} must be smaller than if the charged surface states were absent. This means that the depletion width and the amount of band bending (or the built-in voltage V_{bi}) will be reduced correspondingly

$$V_{bi-illumination}=V_{bi-dark}-\frac{Q_{ss}d}{2\varepsilon_{r}\varepsilon_{0}}. \qquad (4.4)$$

The reduction in V_{bi} under illumination causes a reduction in the ϕ_{B} ($\phi_{B}=V_{bi}+V_{n}$, where V_{n} is the energy difference between Fermi level and the bottom of the conduction band). This process can be described as a light induced change in the Fermi-level partial pinning (or change in the position of the characteristic charge neutrality energy). Assuming $N_{ss}=5\times10^{9}$ cm^{-2}, and d ($V\geqq0$), Katz *et al.* obtain a reduction in ϕ_{B} of $\Delta\phi_{B}$~50 meV, for the amount of accumulated holes shown earlier. At a reverse bias of 5 V we get $\Delta\phi_{B}$~70 meV. Therefore, the current under illumination is

$$I_{illumination}=AA^{*}T^{2}\exp\left(-\frac{\phi_{b}-\Delta\phi_{b}}{kT}\right)\exp(qV/nkT)[1-\exp(-qV/kT)]-I_{ph}. \qquad (4.5)$$

Applying Eqs. (4.1) and (4.5), the responsivity will be

$$\Re = \frac{\left[\exp\left(\frac{\Delta\phi_b}{kT}\right) - 1\right] I_{dark} - I_{ph}}{W}. \tag{4.6}$$

where I_{ph} is the photocurrent due to photogenerated electron-hole pairs. According to Eq. (4.6) there are two mechanisms contributing to the photoresponse. The first is the "primary current" maintained by carriers optically generated in the depletion region, I_{ph}. The "secondary current" is due to the lowering of the Schottky barrier caused by illumination and trapping at interface states. This mechanism is responsible for the gain. For forward bias, and reverse bias higher than 1 V, the secondary current is much higher then the primary current.

The photoresponse increase with voltage, under reverse bias (see the inset of Fig. 4.5), is caused by the dependence of barrier reduction on the bias [Eq. (4.4)], and the increase in dark current. Field dependence barrier height, or tunneling, may be responsible for the current increase in reverse bias. For these mechanisms the photoresponse caused by barrier height reduction has the same bias dependency, as the dark current itself.

4.3.4 Currents under illumination with various power density

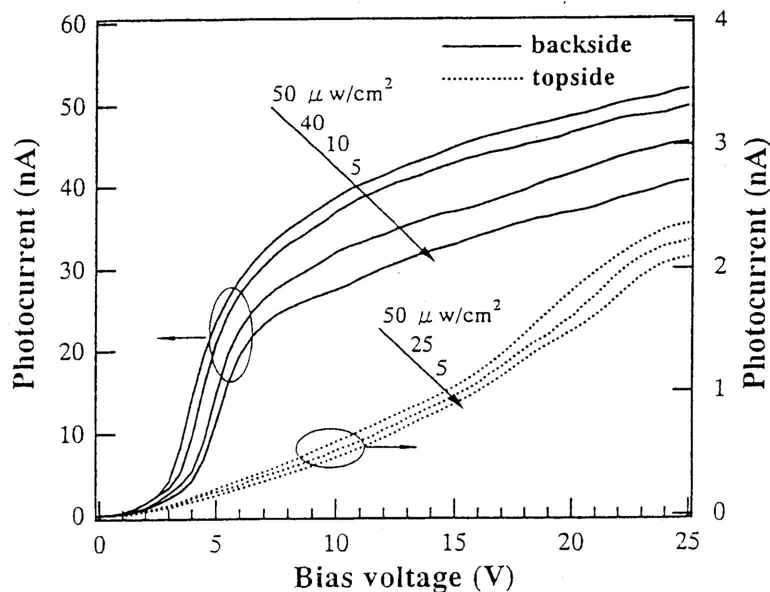

Fig. 4.6. Top- and back-illuminated photocurrent-voltage characteristic under the different irradiance densities of the irradiance with wavelength of 350 nm.

In Fig. 4.6, the photogenerated currents with the dark current subtracted are shown. The

wavelength of the irradiance light is 350 nm. For the Schottky contacts without the effect of hole accumulation, the *I-V* curve should be horizontal in the regime of photocurrent saturation. The rising photocurrents with increasing voltages under top and back illumination indicate the occurrence of electron injection. Note also that the voltage at which saturation current is achieved shows dependence on the irradiance density, establishing the presence of the charge-screening effect due to the hole accumulation. In the case of back illumination, the incident UV light generates a large density of carriers immediately beneath the electrodes, and then a large excess potential drop resulting from the accumulation of holes occurs near the cathode contacts, leading to a vast injection of electrons. Unlike the back illumination, the top-illuminated photoexcited carriers are primarily excited in the gap area of the metal finger, drift to the electrodes and contribute to the photocurrent. In this case, the accumulation of holes, we speculate, is mainly due to photoinduced holes collected around the periphery of metal electrodes. For this reason, the excess hole density is much less than the case of back illumination, leading to a much smaller electron injection. It should be noted that the charge-accumulation effect is indicated to result in a slower transit time of the photocurrent; however, the high ratio of photocurrent to dark current obtained under back illumination is still of interest in its ability to detect low-intensity UV light.

4.4 SUMMARY

In conclusion, back-illuminated GaN-based MSM-PDs operating in the UV region were fabricated and characterized. These photodetectors exhibited low dark currents and high responsivities. Spectral characterization exhibits a visible rejection ratio of four orders of magnitude under 5 V bias and irradiance density of 5 $\mu W/cm^2$. The responsivity recorded at 350 nm is 16.5 A/W, which is much larger than the value (0.32 A/W) of top illumination. The optical characteristics of the devices showed evidence of high internal gain. The likely mechanism responsible for internal gain was proposed to be the electron injection due to the hole accumulation

effect. The high responsivity of back illumination was ascribed to the enhancment of the electron injection by a high-density optically generated charge. The back illuminated MSM-PD with such high responsivity may have potential applications in flame sensors and engine monitoring, where the speed is not the primary issue.

References

[1] J. C. Carrano, T. Li, P. A. Grudowski, C. J. Eiting, R. D. Dupuis and J. C. Campbell, J. Appl. Phys. **83**, 6148 (1998).

[2] D. Walker, E. Monroy, P. Kung, J. Wu, M. Hamilton, F. J. Sanchez, J. Diaz and M. Razeghi, Appl. Phys. Lett. **77**, 274 (2000).

[3] C. Pernot, A. Hirano, M. Iwaya, T. Detchprohm, H. Amano and I. Akasaki, Jpn.J. Appl. Phys. **38**, L487 (1999).

[4] F. Hieronymi, E. H. Bottcher, E. Droge, D. Kuhl, St. Kollakowski and D. Bimberg, Electron. Lett. **30**, 1247 (1994).

[5] M. C. Hargis, S. E. Ralph, J. Woodall, D. McInturff, A. J. Negri and P. O. Haugsjaa, IEEE Photon. Technol. Lett. **8**, 110 (1996).

[6] A. T. Ping, A. C. Schmitz, M. A. Khan and I. Adesida, Electron. Lett. **32**, 68 (1996); A. C. Schmitz, A. T. Ping, M. Asif Khan, Q. Chen, J. W. Yang and I. Adesida, Semicond. Sci. Technol. **11**, 1464 (1996).

[7] K. J. Duxstad, E. E. Haller and K. M. Yu, J. Appl. Phys. **81**, 3134 (1997).

[8] S. V. Averine, A. Kohl, R. Muller, J. Wisser and K. Heime, Solid-State Electron. **36**, 61 (1993).

[9] H. Hasegawa, Y. Koyama and T. Hashizume, Jpn.J. Appl. Phys. **38**, 2634 (1999).

[10] J. B. D. Soole and H. Schumacher, IEEE J. Quantum Electron. **27**, 737 (1991).

[11] M. Ito and O. Wada, IEEE J. Quantum Electron. **22**, 1073 (1986).

[12] M. Klingenstein, J. Kuhl, J. Rosenzweig, C. Moglestue, A. Hulsmann, Jo. Schneider and K. Kohler, Solid-State Electron. **37**, 333 (1994).

[13] S. F. Soares, Jpn.J. Appl. Phys. **31**, 210 (1992).

[14] O. Katz, V. Garber, B. Meyler, G. Bahir, and J. Salzman, Phys. Stat. Sol. (a) **188**, 345 (2001).

[15] L. Leung, A. F. Wright, and E. B. Stechel, Appl. Phys. Lett. **74**, 2495 (1999).

[16] D. C. Look and J. R. Sizelove, Phys. Rev. Lett. **82**, 1237 (1999).

CHAPTER 5
GaN MSM UV Photodetector with Recessed Electrodes

5.1 INTRODUCTION

Over the past few years, ultraviolet (UV) photodetectors (PDs) based on III-nitride compounds have attracted considerable interest in military and commercial applications. A number of reports on GaN or AlGaN photoconductive,[1] Schottky barrier,[2] *p–n* junction,[3] *p-i-n* structure,[4] metal semiconductor metal (MSM) structure,[5,6] and avalanche photodiode[7] UV detectors have been reported in the literature. Recent studies on Schottky MSM photodiodes based on GaN or AlGaN have demonstrated their superior performance in terms of response speed, quantum efficiency, and device noise. Moreover, compared with other photovoltaic photodiodes such as Schottky barrier and *p-i-n* UV PDs, their fabrication is simple and compatible with the field-effect transistor (FET) process. Conventionally, the MSM-PD is a planar structure consisting of two interdigitated electrodes on a semiconductor surface. The planar structure, however, usually brings about problems of the electric field being nonuniform between the two planar contacts and the electric field strength falling off rapidly with increasing distance from the electrodes. Despite recent efforts to improve the quality of the photoactive III-nitride epilayer,[8,9] there have been few studies on the improvement of this simple photodiode structure by changing the electrode configuration. It is known that a key factor influencing the efficiency and speed of MSM-PDs is the rapid sweepout of photogenerated carriers associated with a high electric field strength and short conduction path. At below reach-through bias conditions the carrier collection time can be prohibitively long. Even under higher bias, the carrier collection time can still remain long due to delays from carriers generated deep within the semiconductor layer. Increasing the bias does not always provide an acceptable solution to the delay problem. As the applied bias increases, the dark current, due to thermionic emission and tunneling at the Schottky contacts, increases strongly. Therefore,

alternative device designs should be proposed. A recessed-electrode structure, compared with the conventional planar one, has the potential to provide a uniform and enhanced electric field within the light absorption region of the MSM-PD. Thus, the motivation for this work is to fabricate and characterize GaN-based MSM-PDs with recessed electrodes.

5.2 EXPERIMENTAL PROCEDURES

The GaN films were grown on (0001) sapphire by the horizontal atmospheric pressure metalorganic chemical-vapor deposition (MOCVD) method. Trimetylgallium (TMG) and ammonia (NH_3) served as precursors, and H_2 was used as the carrier gas. Before the film growth, the substrate was heated at 1180℃ in a stream of hydrogen for 10 min. Epitaxial growth started with the deposition of a 30-nm-thick GaN buffer layer at 500℃, followed by deposition of a 0.5-μm -thick unintentionally doped epitaxial GaN layer at 1130℃. Interdigital patterns with the active area of $100 \times 105\ \mu m^2$, finger width of 5 μm and gap spacing of 10 μm were defined by photolithography using a Hg-Xe lamp source. The exposed parts of the GaN epilayer were recessed by self-bias boron trichloride (BCl_3) plasma reactive-ion-etching (RIE). The etching process was carried out under a 10 W RF power with the BCl_3 gas flow rate of 10 sccm. The chamber pressure was maintained at 3.0 Pa during etching. A recessed depth of 0.25 μm was selected, which is sufficiently deeper than the absorption depth ($1/\alpha$=0.12 μm in our case, corresponding to an absorption coefficient value of $\alpha = 8.23 \times 10^4\ cm^{-1}$ at a wavelength of 360 nm) of the incident UV light. In order to recover the damage induced by RIE, the samples were dipped in boiling aqua regia for 10 min and annealed at 750°C in N_2 ambient for 30 min. Schottky contacts (80 nm Pd and 100 nm Au) were subsequently deposited by electron-beam evaporation and formed by an etching process. The resulting cross-sectional structure of the recessed-electrode MSM-PDs is depicted in Fig. 5.1(b). For comparison, conventional planar MSM-PDs were also fabricated on the same wafer with the structure shown in Fig. 5.1(a).

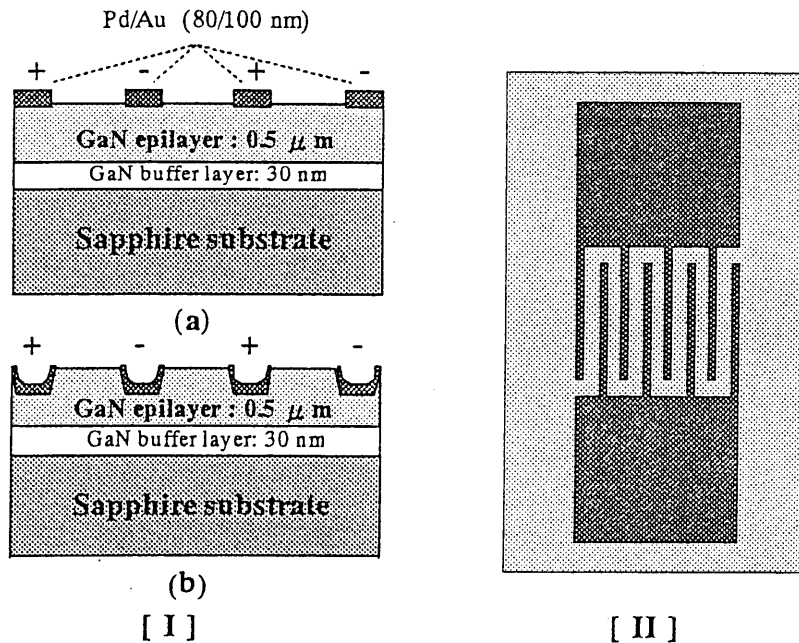

Fig. 5.1. [I] Schematic cross sections of the GaN-based MSM-PDs with (a) planar electrodes (b) recessed electrodes; [II] Top view of MSM-PD showing the interdigitated geometry

5.3 CHARACTERISTICS ANALYSIS

5.3.1 Current– voltage behavior

Measurements of the dark current–voltage (I–V) characteristics of the MSM-PDs were performed with an HP4145B parameter analyzer at room temperature. The typical I-V characteristics for both

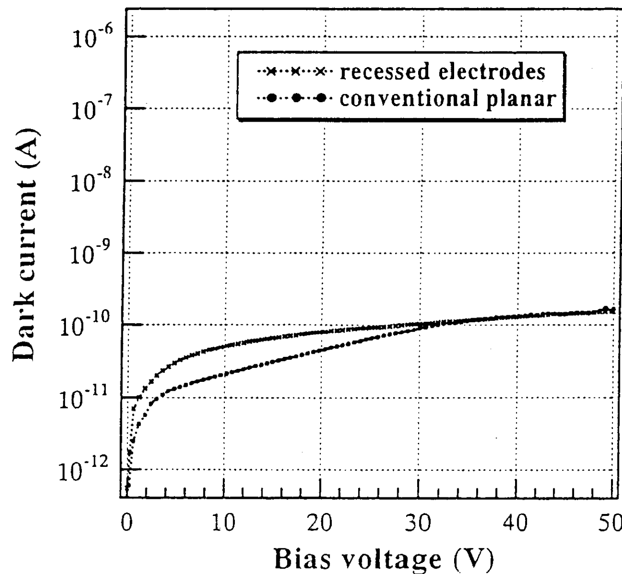

Fig. 5.2. Dark I-V characteristics of the conventional and recessed-electrode MSM-PDs at room temperature.

types of MSM-PDs are compared in Fig. 5.2. At a typical operating bias of 10 V, the leakage currents are 21.4 pA and 50.8 pA for conventional and recessed-electrode MSM-PDs, respectively. To evaluate the fabricated Schottky contacts, we formed satellite Ohmic contacts by alloying indium dots directly on the GaN epilayer.

5.3.2 Analysis of series resistance effects on I- V characteristics

The current-voltage relationship for a metal-semiconductor Schottky diode, based on the thermionic field emission model, is given by the following equations:[10]

$$I = I_0 \exp(qV/nkT)[1-\exp(-qV/kT)], \quad (5.1)$$

where I is measured current, V is voltage applied across the junction, n is the ideality factor that describes departure from the ideal diode equation for reverse bias as well as forward bias. The prefactor I_0 is the extrapolated saturation current given by

$$I_0 = AA^{**}T^2 \exp(-q\phi_B/kT), \quad (5.2)$$

Under forward bias (qV>3 kT), Eq. (5.1) reduces to the familiar form often used to determine I_0,

$$I = I_0 \exp(qV/nkT). \quad (5.3)$$

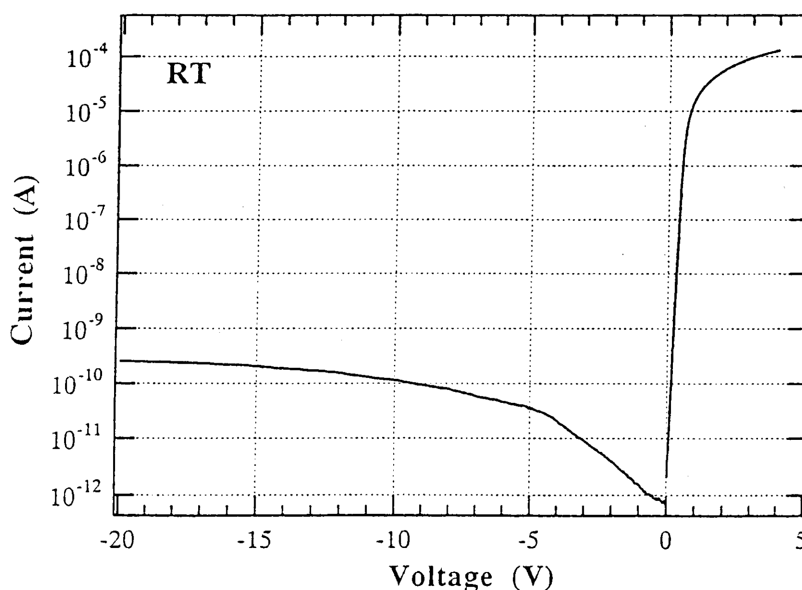

Fig. 5.3. Current-voltage characteristics of a (Au/Pd)/i-GaN Schottky diode. (The Schottky contact is one electrode of the MSM-PD, and the ohmic contact is the satellite indium dot.)

A semilog plot of I vs V yields a linear relation where the intercept at V=0 is I_0 and the slope is

q/nkT. Due to the high current under forward bias, these measurements are relatively immune to the effects of leakage paths. However, the high series resistance R_s, of the semiconductor (such as GaN) film limits the forward current and causes departures from linearity over much of the forward region, as evident in Fig. 5.3. Thus, accurate determination of I_0 and n cannot be obtained from the plot due to the effect of series resistance.

Series resistance has been observed to dominate current conduction processes in large-band-gap semiconductor materials and has been reported to affect I-V measurements on diamond films by other research groups. The series resistance contributes a prominent component because, at large currents, the voltage drop occurring across the series resistance of the diamond film is large and occurs in addition to the voltage drop across the junction. Therefore, the correct voltage across the junction is considered as $V- IR_s$, where R_s, is the series resistance. Thus, the contribution of R_s, to the experimental I-V data can be subtracted from the thermionic field emission model of Eq. (5.3) as

$$I = I_0 \exp[q(V - IR_s)/ nkT], \tag{5.4}$$

Differentiating Eq. (5.4), one gets the following equation:

$$I = \frac{1}{R_s}\left(\frac{dV}{d\ln(I)} - \frac{nkT}{q}\right), \tag{5.5}$$

The equation implies that if a plot of I vs $d\,V/d\,In(I)$ yields a straight line, then R_s, can be obtained from l/slope of that linear behavior. The I vs $d\,V/d\,In(I)$ characteristics are shown in Fig. 5.4. (a). The plot is indeed linear for the forward voltage range investigated. One can also obtain the series resistance of a Schottky diode from its forward bias I-V data using the approach described by Norde[11]or Lien, So, and Nicolet.[12]

Once the series resistance at a particular temperature has been evaluated by this method, its contribution to the experimental I-V data can be subtracted from Eq. (5.5). Figure 5.4.(b) shows a $In(l)$ vs $(V\text{-}IR_s)$ plot. The curves are linear over the entire voltage range. Accurate values of n and I_0 were then determined.

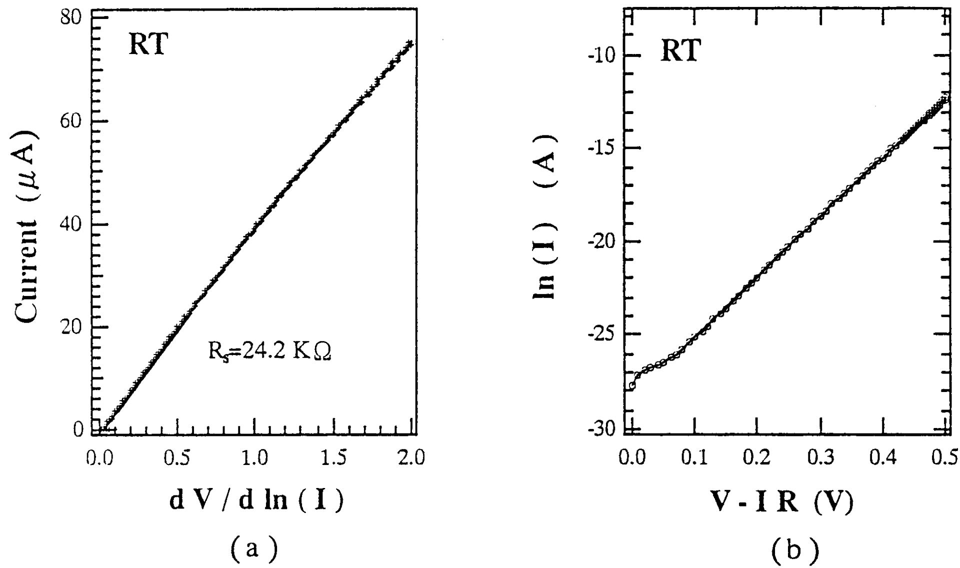

Fig. 5.4. Plots of I vs d V/d ln(I) of the Schottky diode which the Schottky contact is one planar electrode of MSM-PD and the ohmic contact is a satellite indium dot. The slope of linear plot indicates a constant series resistance value.

The prefactor I_0 can also be extracted from the reverse *I-V* characteristics through a semilog plot of $I/\{1 - \exp[-q(V-R_s)/kT]\}$ vs $(V-IR_s)$, obtained from Eq. (1) taking R_s into consideration. Figure 5.5 shows the *I-V* characteristics of the Schottky diode plotted in this manner. I_0 is determined from the point where the curves cross the $V= 0$ axis. Due to the low-current densities associated with reverse currents, the measurement is less effected by R_s . As is the case for extrapolation from semilog *I-V* characteristics in forward bias, the value of I_0 can be accurately determined from reverse bias semilog *I-V* since the plot is linear over the entire reverse region for the temperature range investigated. However, due to the heating effect caused by the reverse biasing of the junction, I_0 values obtained from the reverse bias are slightly higher than those obtained from the forward bias region.

These examinations, therefore, indicate that the current conduction of the diode can be modeled by the modified thermionic field emission equation in both the forward bias and reverse bias regimes for the Schottky diode. The diode can be modeled as an Schottky barrier in series with R_s . From the corrected thermionic field emission model, accurate values of n and I_0, can be obtained.

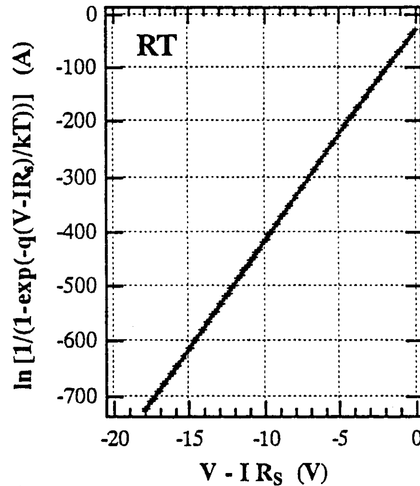

Fig. 5.5. Reverse bias ln(U(l -exp[-q(V-IR_S)lkTJ}) vs (V-IR_s) characteristics of a (Au/Pd)/i-GaN Schottky diode taking series resistances into consideration.

According to the method proposed above, analysis on Pd/Au Schottky contact of MSM-PD shows that the saturation current I_0, ideality factor n and Schottky barrier height ϕ_B are 0.65 pA, 1.05 and 0.85 eV for the planar contact and 1.76 pA, 1.09 and 0.83 eV for the recessed contact, respectively. The degraded ideality factor and barrier height in the case of the recessed Schottky contacts may be related to the near surface damages induced by RIE. This degradation together with the increased junction area of the Schottky contacts led to a higher leakage current in the recessed-electrode MSM-PD. It was also found that the leakage current of the recessed-electrode MSM-PD requires a lower voltage to achieve a saturation "knee" and is less dependent on bias above the so-called knee voltage. This implies an enhanced and uniform electric field distributed through the gap space in the recessed-electrode structure.

5.3.3 Optical properties

The spectral response of the MSM-PD exposed to an irradiation power density of 10 μW/cm^2 is shown in Fig. 5.6. A UV-visible spectrophotometer with a xenon-arc lamp source and a monochromator with a grating of 600 lines/mm were used for these measurements in the range of 450~300 nm. The constant irradiation power density was corrected with a thermopile unit, while the absolute values of responsivity were determined using a calibrated Si detector.

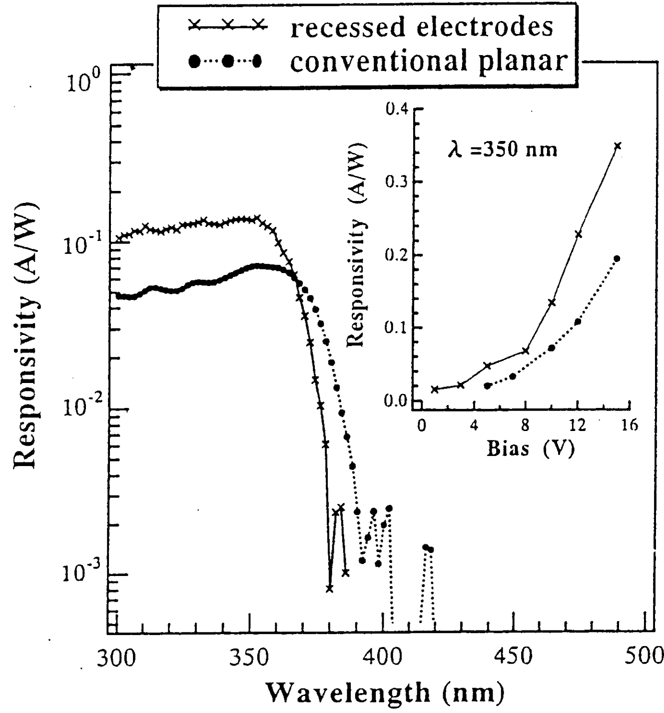

Fig. 5.6. Comparison of the spectral response characteristics of conventional and recessed-electrode GaN MSM-PDs biased at 10 V. The inset shows the variation of responsivities with increasing bias voltage.

For both types of MSM-PDs, the responsivities are quite flat over the band gap and exhibit a sharp cutoff at the absorption edge. Under 10 V bias, the responsivities at 350 nm are 0.134 A/W and 0.071 A/W for the MSM-PDs with and without recessed electrodes, respectively, corresponding to an external quantum efficiency of 47.5% and 25.2%. Taking into consideration the shadowing of the electrodes and the surface reflection of the incident light, the internal quantum efficiency η_{int} is related to the current responsivity $\Re_i$ as shown by

$$\Re_i = \frac{\lambda q}{hc}(1-R)\left(\frac{s}{s+w}\right)\eta_{int}, \tag{5.6}$$

where λ is the wavelength, h is Planck's constant, c is the light velocity, q is the electron charge, R is the power reflectance at the air-GaN interface, s is the gap spacing, and w is the metal finger width.[13] Taking R=21% at 350 nm, s=10 μm and w=5 μm, the internal quantum efficiencies of the planar and recessed-electrode MSM-PDs at various bias voltages of 5, 10, and 15 V were then calculated and are listed in Table 5.1.

Table 5.1. Internal quantum efficiency of the conventional planar and recessed-electrode MSM-PDs at various bias voltage.

Type of Device	Internal Quantum Efficiency (%)		
	5V	10V	15V
conventional	13.5	47.8	130.6
recessed-electrode	31.6	90.2	234.3

It was shown that the internal quantum efficiency was obviously higher for the recessed-electrode MSM-PD. We attribute this to the enhanced electrical field strength in the deep portions of the active layer in the case of the recessed-electrode MSM-PD, which results in efficient sweep-out of photogenerated carriers. Under the applied bias, the depletion region is deepened and widened by the recessed electrodes, the electric field strength in the photoactive region was higher, and the electric field distribution was more uniform. For this reason, the conduction path along the electric field line via which the carriers travel to the electrodes was shortened. As a consequence, the generated electron-hole pairs in the photoactive region could be separated and collected efficiently by the recessed electrodes with less recombination-eliminating effect. It was also found that the responsivity increases as a function of bias voltage, as shown in the inset in Fig. 5.6. These characteristics combined with the internal quantum efficiencies of more than 100% are evidence of some internal gain. The reasons for this internal gain have been discussed in the chapter 4. Here, we would like to simply remark it again.

In the bias range under consideration, both types of MSM-PD are partially depleted; i.e., a low-field diffusion region is present between the two depletion regions of the cathode and anode contacts. As bias increases, the diffusion region decreases due to the increase of the two depletion regions, and the carrier diffusion effect subsequently decreases, leading to a proportionally increased photoconductive gain in the responsivity. Another contribution to the internal gain is generally considered to be the injection of additional electrons at the cathode contacts by photoinduced hole accumulation, leading to an internal quantum efficiency over 100%. The

possible mechanisms responsible for the hole accumulation in GaN-based MSM-PDs have been discussed by Monroy *et al.*.[14] We speculate that the larger internal gain present in the recessed-electrode MSM-PD is due to the improved separation of photogenerated electron-hole pairs leading to an increased density of holes accumulating at the cathode contacts.

5.3.4 C-V-F measurement

If a metal contact to an extrinsic semiconductor results in the formation of a depletion region in the semiconductor adjacent to the contact, the system may be treated as a voltage-dependent capacitance. The depletion region froms a barrier to the flow of mobile charge carriers to from the metal into the semiconductor. Under certain conditions, the height of the barrier and the charge density in the depletion region can be obtained from a measurement of the variation of the capacitance with applied voltage. One such case is that of the Schottky barrier in which it is assumed that the charge density in the depletion region is constant and due only to the ionized donor atoms.

Most commercial capacitance meters measure the capacitance of the diode under test by applying a constant RF voltage , and monitoring the imaginary component of resulting RF current. If there is no series resistance in the equivalent circuit of the diode, the imaginary component of the RF current is directly proportional to the depletion region capacitance. In the presence of series resistance, however, it is straightforward to show that the measured capacitance, C_m, is given by

$$C_m = \frac{C}{1+(\omega R_s C)^2}, \tag{5.7}$$

where C is the actual depletion region capacitance, $\omega$is the measurement angular frequency, and R_s is the series resistance. Clearly $C_m<C$, and one would like to have $(\omega R_s C)^2<<1$. Fig. 5.7 illustrates some of the sources of series resistance encountered in realistic test diode. From Eq. (5.7), it can be seen that there are several possible ways to reduce the effect of series resistance, since its influence is only felt through the product $(\omega R_s C)^2$. Assuming the resistance itself has been reduced as much as possible, one could reduced the capacitance by using test diodes of smaller area. It is

not practical to use diode areas below 10^{-4} cm^2, however, because of the increasing importance of edge-effect and stray-capacitance correction, and the difficulty of measuring such small areas accurately. Another method is to reduce the measurement frequency, but it should be noted that the too low measurement frequency may let singal-to-noise ratio become worse.

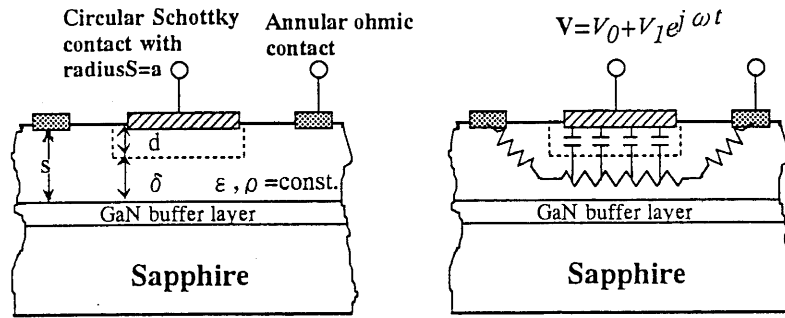

Fig. 5.7. A cross-sectional view of a metallic Schottky contact on an epitaxial semiconductor film with Sapphire substrate. The dashed line indicates the depletion region near the Schottky contact. The depletion-layer capacitance is shown in series with resistances which arise from the undepleted semiconductor and the ohmic contact.

For Schottky barrier MSM-PD, the calculation of the capacitance at zero bias has been introduced in the chapter 2.3. For capacitance-voltage (C-V) characteristic, Sze has shown both theoretically and experimentally that Schottky barrier MSM-PDs have a maximum capacitance when a small positive or negative bias voltage is applied and a local minimum in capacitance at zero bias.[15] This results in a characteristic hump in the C–V curves from such a structure. The maximum arises from the capacitance of a forward biased barrier (anode) at one interface acting in series with a reversed biased barrier (cathode) at the other contact. The total voltage drop across the structure is given by the sum of the voltage drop across the forward biased (V_a) and the reversed biased (V_c) interfaces and any voltage drop that occurs across the bulk of the semiconductor (V_{bulk}) which is a function of the thickness of the semiconductor (t), so that

$$V = V_a + V_c + V_{bulk}(t). \tag{5.8}$$

Sze took the voltage drop across the semiconductor to be zero and showed, using standard expressions for the capacitances of the interfaces that the total capacitance of the structure is given

by

$$C = C_a C_c / (C_a + C_c), \tag{5.9}$$

with
$$C_a = \sqrt{\frac{q\varepsilon N_d}{2(V_{Da} - V_a)}}, \tag{5.10}$$

$$C_c = \sqrt{\frac{q\varepsilon N_d}{2(V_c + V_{Dc})}}, \tag{5.11}$$

where q is the charge of an electron, ε the dielectric constant of the semiconductor, and N_d the doping concentration of the semiconductor. For symmetrical structures, the built-in potential V_D was taken to be the same for the two interfaces ($V_D=V_{Da}=V_{Dc}$). In the limit of small applied voltages ($V<<V_D$), the resultant capacitance reduced to

$$C = \sqrt{\frac{q\varepsilon N_d}{2}}\left(\frac{1}{\sqrt{(V_c + V_{Dc})} + \sqrt{(V_{Da} - V_a)}}\right),$$

$$\approx \sqrt{\left(\frac{q\varepsilon N_d}{8V_D}\right)}\left(1 + \frac{V^2}{32V_D^2}\right), \tag{5.12}$$

Thus, the capacitance of the structure increases initially with bias voltage. At higher voltages most of the voltage drop occurs across the cathode contact. The capacitance

$$C = \sqrt{\left(\frac{q\varepsilon N_d}{2}\right)}\left(\frac{1}{\sqrt{(V + V_D)} + \sqrt{V_D}}\right), \tag{5.13}$$

then decreases with increasing voltage. These two limits imply that the capacitance of the structure goes through a maximum at small voltages resulting in a peak in the C–V. For $V>V_{RT}$, the semiconductor is completely depleted, and the capacitance per unit area is the same as that for a parallel plate condenser. Typically, the measured capacitance for a symmetric MSM structure is symmetrical with respect to the voltage axis. For voltages large than $|V_{RT}|$ the capacitance should remain constant.

Capacitance-voltage-frequency (C-V-F) measurements were carried out using an HP4284A

LCR meter with frequencies ranging from 500 Hz to 1 MHz. For the MSM-PD structure with the highly resistive epilayer, the series resistance (R_s) may introduce error in the measured capacitance. It is generally accepted that the *C-V* measurement should be questioned unless $\omega R_s C << 1$. In our case, the value of R_s extracted from the forward *I-V* characteristics of the Schottky diodes is in the range of 40 to 60 $K\Omega$. Note that this value may be larger than that in the MSM-PD because of the longer distance between the Ohmic and Schottky contacts (~100-250 μm). To reduce the effect of R_s on *C-V* characteristics, a useful method is to lower the test frequency.

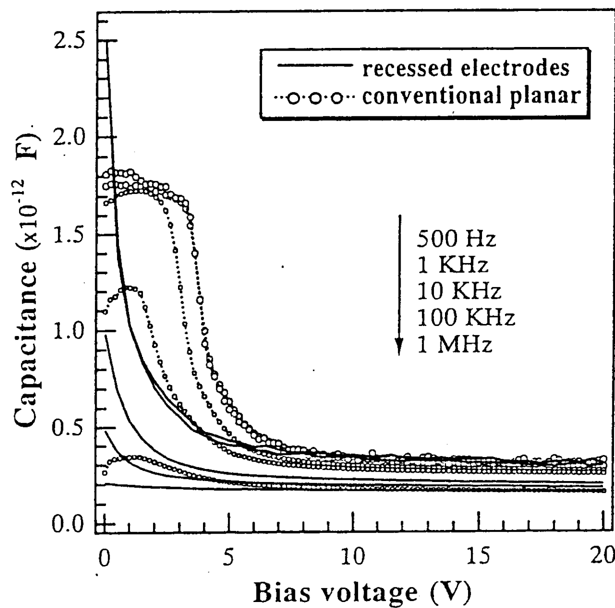

Fig. 5.8. C-V-F characteristics of the conventional and recessed-electrode MSM-PDs.

Figure 5.8 shows the *C-V-F* characteristics of the conventional and recessed-electrode MSM-PDs. It was observed that the *C-V* curves at 500 Hz are very close to the curves at 1 KHz. Assuming that $C \leq 3$ pF, the maximum value of $\omega R_s C$ is 1.13 at 1 MHz, while it is only 1.13×10^{-3} at 1 KHz. We therefore consider that the R_s induced error can be neglected when the frequency ≤ 1 KHz. For the planar MSM-PD, the capacitance trace increases from its zero-bias value to a maximum and then decreases monotonically, which is in agreement with the typical curve trend reported in the literature. The trace for the recessed-electrode MSM-PD, as compared to the planar device, starts at a larger zero-bias value, decreases more rapidly and flattens out at lower bias. This trend supports the hypothesis that the electric field in the active region is enhanced due to the

recessed electrodes. In this case, the voltage drop across the depletion region of the Schottky contacts under the same applied voltage will be larger in the recessed structure than in the planar structure, leading to a faster extension of the depletion region (i.e., a faster capacitance decrease) with increasing bias voltage. As the frequency is increased, the capacitance dependence on bias becomes less pronounced due to the effect of large R_s. In the case of the recessed-electrode MSM-PD, the C-V curve exhibits a downthrow when the frequency is varied from 1 KHz to 10 KHz. This downthrow may be due to the RIE-induced defects which partially compensate the depletion region.[16] The anomalous C-V characteristics at high frequencies are therefore caused by a combination of the effects resulting from large R_s and RIE-induced defects.

5.5 SUMMARY

In summary, GaN-based MSM-PDs with recessed electrodes have been fabricated and their characteristics have been compared with the conventional planar structure. The photodiodes exhibited low leakage current and capacitance. An enhanced responsivity was found in recessed-electrode MSM-PDs with a peak value of 0.134 A/W under the irradiation power density of 10 μW/cm^2, corresponding to an internal quantum efficiency of 90.2%, which is a 42.4% improvement over that of conventional MSM-PDs. The improvement was ascribed to the enhanced and uniform electric field in the photoactive regions due to the recessed electrodes.

References

[1] D. Walker, X. Zhang, A. Saxler, P. Kung, J. Xu and M. Razeghi, Appl. Phys. Lett. **70** (1997) 949.

[2] A. Osinsky, S. Gangopadhyay, B. W. Lim, M. Z. Anwar and M. A. Khan, Appl. Phys. Lett. 72 (1998) 742 .

[3] D. V. Kuksenkov, H. Temkin, A. Osinsky, R. Gaska and M. A. Khan, Appl. Phys. Lett. 72, (1998) 1365.

[4] D. Walker, A. Saxler, P. Kung, X. Zhang, M. Hamilton, J. Diaz and M. Razeghi, Appl. Phys. Lett. 72 (1998) 3303.

[5] D. Walker, E. Monroy, P. Kung, J. Wu, M. Hamilton, F. J. Sanchez, J. Diaz and M. Razeghi, Appl. Phys. Lett. **74** (1999) 762.

[6] T. Li, D. J. H. Lambert, A.L. Beck, C. J. Collins, B. Yang, M. M. Wong, U. Chowdhury, R. D. Dupuis and J. C. Campbell, Electron. Lett. **18** (2000) 1518.

[7] J. C. Carrano, D. J. H. Lambert, C. J. Eiting, C. J. Collins, T. Li, S. Wang, B. Yang, A. L. Beck, R. D. Dupuis and J. C. Campbell, Appl. Phys. Lett. **76** (2000) 924.

[8] C. Pernot, A. Hirano, M. Iwaya, T. Detchprohm, H. Amano and I. Akasaki, Jpn. J. Appl. Phys. **38** (1999) L487.

[9] M. Razeghi, P. Sandvik, P. Kung, D. Walker, K. Mi, X. Zhang, V. Kumar, J. Diaz and F. Shahedipour, Mater. Sci. & Eng. **B74** (2000) 107.

[10] H. C. Card and E. H. Rhoderick, J. Phys. D **4**, 1589 (1971).

[11] H. Norde, J. Appl. Phys. **50**,5052 (1979).

[12] C. D. Lien, F. C. T. So, and M.-A. Nicolet, IEEE Trans. Electron Devices **ED-31**, 1502 (1984).

[13] J.B.D. Soole and H. Schumacher, IEEE J. Quantum Electron **QE-27**, 737 (1991).

[14] E. Monroy, F. Calle, E. Munoz and F. Omnes, Phys. Status Solidi (a) **176** (1999) 157 .

[15] S. M. Sze, D. J. Coleman and A. Loya, Solid-State Electron. **14** (1971) 1209 .

[16] See, for example, E. H. Rhoderick and R. H. Williams, *Metal-Semiconductor Contacts* (Clarendon, Oxford, 1988).

CHAPTER 6
Summary and Future Trends

6.1 SUMMARY

The work of this dissertation is focused on two aspects. At first, it is started with an investigation on the optical properties of $Al_xGa_{1-x}N$, including the optical absorption in n-type GaN and the Al composition dependence of bandgap in ternary AlGaN alloys. Both of them are the most important properties in design and characterization of $Al_xGa_{1-x}N$ UV photodetectors. Based on the knowledge of these properties, the second part of this work means the fabrication and characterization of GaN MSM-PD were performed with an object to improve the performance especially the responsivity of this type photodetector. Here, we summarized this dissertation as the follows.

In chapter 1, the background of the UV radiation, the state-of-the-art $Al_xGa_{1-x}N$ based UV photodetector and its possible application were discussed.

In chapter 2, the basic operating principles of the metal-semiconductor photodetector including Schottky barrier photodiode and Schottky MSM-PD were presented. Generally the behavior of these devices results from the absorption of UV radiation with consequent electronic effect in GaN. For this reason, the optical absorption process in undoped and Si-doped n-type GaN was discussed. The following discussions on the photoresponse mechanism showed that the optical parameter of interest is the absorption coefficient, $\alpha(\lambda)$, and the electrical parameters of interest are minority carrier diffusivity, D, and diffusion length, L. At last, the performance figures and their analysis method, which can be utilized in understanding the operation of devices and the optimization of performance, were also presented. .

In chapter 3, the research works on optical properties of the ternary $Al_xGa_{1-x}N$ alloys are reported. The normal-incidence reflectance measurement was employed to obtain the free exciton transition energy (E_{FX}) of AlGaN alloys in $Al_xGa_{1-x}N$/GaN/Sapphire heterostructure grown by MOCVD. It was found that the thickness variation of the AlGaN layer may cause a noticeable

change in the line shape of reflectance spectrum and impede the identification of the desired excitonic position. By using a reflection model of two absorbing layers with a transparent substrate, the experimental reflectance spectra were theoretically simulated and utilized to explain the reflection mechanism in $Al_xGa_{1-x}N/GaN$ heterostructures. On the basis of the above analysis, the feasibility of the reflectance measurement for such heterostructures is confirmed. At room temperature, the E_{FX}s obtained from the fitting showed an excellent agreement with the corresponding peak energies in the photoluminesence spectra. Furthermore, at the optical energy position about 100 meV above the E_{FX}, the spectral feature of exciton-LO phonon interaction was observed in the reflectance spectrum record for low Al composition ($x \leqq 0.16$). Using the Al mole fraction derived from x-ray diffraction measurement, the bowing parameter of the epitaxial AlGaN layer was determined. In the range of $0 \leqq x < 0.3$, the resulting bowing parameter shows a downward value of 0.53 eV.

In chapter 4, the fabrication and characterization of back illuminated MSM-PDs based on GaN grown on (0001) sapphire were introduced. The photodetector with a thin GaN layer of 0.3 μm exhibited low dark current with a saturation value of 2.06 pA. A visible rejection of more than four orders of magnitude was observed in the spectral responsivity under 5 $\mu W/cm^2$ irradiance at 5 V bias. The responsivity was 16.5 A/W at a wavelength of 350 nm, which is 55 times that of the top illumination case. The results imply the presence of high internal gain under back illumination, due to the high density of charge generation.

In chapter 5, GaN-based MSM-PDs with a recessed-electrode structure have been fabricated and characterized. The photodiodes exhibited low leakage currents with a typical value of 51 pA at 10 V. Spectral response revealed a responsivity up to 0.14 A/W at 350 nm under 10 V bias, corresponding to an internal quantum efficiency of about 90%, which is a 55.6% improvement over that of conventional MSM-PDs with planar electrodes. The improvement was attributed to the enhanced and uniform electric field due to the recessed electrodes in the photoactive region, leading to a more efficient carrier collection.

6.2 FUTURE TRENDS

Despite the remarkable developments in $Al_xGa_{1-x}N$-based UV photodetectors, true solar-blind detectors with very low noise levels and signal amplification have not yet been reported. Past research works on these devices show that several factors, just as in development of other $Al_xGa_{1-x}N$-based optoelectronics (LED and LD etc.), have played a key role in realizing high-performance photodetectors, such as better control over the residual oxygen concentration in the MOCVD growth process [especially by use of improved purity precursors, NH_3 , and $(CH_3)_3Ga$] and use of optimized buffer layers as a template for active layer growth; the development of low defect density epitaxy, using the ELO or quasi-GaN-substrate approaches; ability to grow high quality AlGaN with high Al-content; better stoichiometry control to avoid high n-type doping backgrounds in epitaxial material; improved processing methods in the areas of ohmic and rectifying contacts, dry etching, facet coating, cleaving and implant activation and isolation, and finally in device design. With consideration of these factors, the further research works will be concentrated on the following aspects.

(I) The main issue in the fabrication of UV detectors seems to be one of improving material purity and quality. In order to establish true solar-blind photodetector, high-quality and well-controlled ternary $Al_xGa_{1-x}N$ is essential. In n-type $Al_xGa_{1-x}N$, minority hole diffusion length L_p decreases with increasing doping level. A decrease of L_p is explained by a decrease in the carrier mobility (diffusivity), μ_n, due to ionized impurity scattering.[1] Significant improvement in the short-wavelength response will result if the minority carrier lifetime can be increased towards its radiative limit in material to which a minority carrier-blocking contact can be applied (as explained in the chapter 2).

Currently, there are still no widely available lattice-matched substrates for the growth of wurzitic GaN. As a result, most materials today still have high threading dislocation (TD) densities. It is indicated that minority carrier recombination, taking place at dislocation, decrease the minority

carrier lifetime, and therefore, diffusion length.[2,3,4] Recently, Akasaki research group of Meijo university has succeeded in reducing both etch pit density and dislocation density to a great extent by insertion of the second LT-buffer layer between a high-temperature (HT) grown GaN on sapphire.[5,6] Crack-free and high-quality thick $Al_xGa_{1-x}N$, with x ranging from 0 to 1, has been grown on sapphire, using low-temperature interlayer. The low-temperature AlN interlayer reduces tensile stress during the growth of $Al_xGa_{1-x}N$, while simultaneously improving the crystalline quality. Cross-sectional TEM showed that by using the multi-step buffer layers dislocation density in GaN decreased to mid 10^7 cm^{-2}, which is one to two orders of magnitude lower than those of conventional single LT-buffer layer method.[7]

Lateral epitaxial overgrowth (LEO) was used to produce areas of low dislocation density in close proximity to areas with the high dislocation density typical for growth on sapphire. For Schottky barrier photodiode, an improvement of one order of magnitude in the UV/visible contrast has been observed, in comparison with devices on standard GaN on sapphire. The significantly lower residual doping concentration reduces markedly the leakage current, and increases the detector bandwidth.[8] A comparison for *p–i–n* $Al_xGa_{1-x}N$ photodiode demonstrates the use of LEO GaN can significantly improve the photodetector noise performance and high-frequency response.[9] This procedure and its many variations[10, 11] will continue to be advanced and simplified, improving the quality of GaN films on inexpensive, large area substrates, and reducing the process costs, and, will be important until GaN substrates become available.

It is speculated that incremental improvements in crystal quality of $Al_xGa_{1-x}N$ film quality on both sapphire and SiC substrates will continue to be made as epitaxial growth processes are refined, and, the fabrication and characterization of UV photodetector on improved $Al_xGa_{1-x}N$ epilayer will thus continue to be one of the future research trends.

Although the well-established process technology for GaN epitaxy on sapphire and silicon carbide ensures that these will remain the most common substrates for the foreseeable future, efforts should still be made to grow large GaN crystals. If GaN substrates become available, the

quality of the epilayers can be improved. Point defects and dislocation density will decrease and there will be an overall improvement in the device performance. On the other hand, in order to accomplish integration of III–nitride photodetectors with Si electronics, these devices will have to be grown locally on an already processed Si chip. Some literatures have reported the UV photodetectors fabricated on $Al_xGa_{1-x}N$ grown on the Si substrate.[12] The results show that the performance is still limited by the quality of $Al_xGa_{1-x}N$ which need to be improved in the days ahead.

In addition to growing GaN films with low defect densities, another key requirement for fabricating devices is the ability to precisely control the desired electrical properties of the thin film. In general, wide bandgap semiconductors are difficult to dope due to native defects. When the enthalpy for defect formation is lower than the band gap energy, the probability of generating a defect increases with the bandgap, i.e. the energy released by donor-to-acceptor transition. There is an urgent need to find acceptors with a lower activation energy to improve *p* doping and hole mobility. If heavier *p* doping becomes possible, it will help in solving the problem of making ohmic contacts to the *p*-type nitrides.[13]

(II) While further improvements in the $Al_xGa_{1-x}N$ quality can be expected to enhance device operation, further device advances will also require improved processing technology. Owing to their wide bandgap nature and chemical stability, GaN and related materials present a host of device processing challenges, including difficulty in achieving reliable low-resistance p-ohmic contacts, lack of efficient wet etch process, generally low dry etch rates and low selectivity over etching masks, and dry etch damage. These problems constitute an obstacle to successful demonstration and commercialization of some $Al_xGa_{1-x}N$-based photodetectors, such as phototransistors, whose performance are much more affected by the immature fabrication techniques. To fully exploit these device applications, a number of critical advances are necessary in the areas of high temperature thermal processing, Ohmic contact to p-type material, dry etching process, and device passivation.

If *p-n* junction varieties are to be used, high *p*-doping in such a high mole fraction AlGaN is no

easy task and none has been demonstrated. Doping efficiency of donors and acceptors decreases drastically as the concentration of Al and band gap of AlGaN increase. The ionization energy of Si in AlGaN increase from 20 to 54 meV for Al concentration of about 20%. No p-type conductivity in AlGaN has been achieved for more than 13% Al. Good ohmic contacts on n-type GaN can now be made but contacts on p-type GaN continue to be a problem. Schottky barrier varieties may remove the requirement of p-doping. However, if avalanche photodiodes (APDs) are pursued for their advantages of high-speed, high-sensitivity and much-needed gain, as required by systems applications, the Schottky barrier varieties may not be as successful as the p-n junction varieties have been in avalanche photodiodes based on conventional compound semiconductors. Moreover, if one very little is really known about the ionization coefficients of electrons and holes in GaN and its alloys. The calculations are frustrated by the lack of reliable data on the properties (such as complete band structure) of these materials. To date, there have been few reports on the GaN-based APDs.[14,15] The development of $Al_xGa_{1-x}N$ APDs has been hampered by the formation of microplasmas due to defects in the material.[16] Its fabrication will be treated as a remaining challenge in the future research work.

(III) The lack of knowledge of physics parameter is not only limited in the design of avalanche photodiodes. There is also a need for experimental data on the Al-mole-fraction dependence in the ternary $Al_xGa_{1-x}N$ system of the absorption coefficient, the refractive index, the minority carrier mobility and life time and on the band offsets in heterojunction formed from materials within the ternary system. In addition, the calculation of the minority carrier diffusion length L, via $L = \sqrt{D\tau}$, presents the greatest uncertainty owing to the almost complete lack of knowledge of the minority carrier lifetime, τ.

It comes with no doubt that if these problems are solved, many more devices will be commercialized. Researchers working in this area are looking forward to new exciting developments in the next few years.

References

[1] S.M. Sze, *Semiconductor Device Physics and Technology*, New York: Wiley; 1985.

[2] Z.Z. Bandic, P.M. Bridger, E.C. Piquette and T.C. McGill, Solid-State Electron **44**, 221 (2000).

[3] P.M. Bridger, Z.Z. Bandic, E.C. Piquette and T.C. McGill, Appl. Phys. Lett. **73**, 3438 (1998).

[4] L. Chernyak, A. Osinsky, G. Nootz, A. Schulte, J. Jasinsky, M. Benamara, Z. Liliental-Weber, D.C. Look and R.J. Molnar, Appl. Phys. Lett .**77**, 2695 (2000).

[5] M. Iwaya, S. Terao, N. Hayashi, T. Kashima, H. Amano, and Isamu Akasaki, Appl. Surf. Sci.**159–160**, 405 (2000).

[6] S. Kamiyama, M. Iwaya, N. Hayashi, T Takeuchi, H. Amano, I. Akasaki, S. Watanabe, Y. Kaneko and N. Yamada, J. Crystal Growth **223**, 83 (2001).

[7] H. Amano and I. Akasaki, Optical Materials **19**, 219 (2002).

[8] E. Monroy, F. Calle, E. Munoz, B. Beaumont, F. Omnes and P. Gibart, Electron. Lett. **35**, 1488 (1999).

[9] G. Parish, S. Keller, P. Kozodoy, J.P. Ibbetson, H. Marchand, P.T. Fini, S.B. Fleischer, S.P. DenBaars, U.K. Mishra and E.J. Tarsa. Appl. Phys. Lett. **75**, 247 (1999).

[10] B. Beaumont, Ph. Vennegures and P. Gibart. Phys. Stat. Sol. (b) **227**, 1 (2001).

[11] K. Hiramatsu. J. Phys: Condens. Matter **13**, 6961 (2001).

[12] J. L. Pau, E. Monroy, E. Munoz, F. B. Naranjo, F. Calle, M. A. Sanchez-Garcia and E. Calleja, J. Crystal Growth **230**, 544 (2001); J. L. Pau, , E. Monroy, M. A. Sanchez-Garcia, E. Calleja and E. Munoz, Mater. Sci. Eng. **B93**, 159 (2002).

[13]S. C. Jain, M. Willander, J. Narayan, R. Van Overstraeten, J. Appl. Phys. **87**, 965 (1999).

[14] K. A. McIntosh, R. J. Molnar, L. J. Mahoney, A. Lightfoot, M. W. Geis, K. M. Molvar, I. Melngailis, R. L. Aggarwal, W. D. Goodhue, S. S. Choi, D. L. Spears, and S. Verghese, Appl.

Phys. Lett. **75**, 3485 (1999).

[15] J. C. Carrano, D. J. H. Lambert, C. J. Eiting, C. J. Collins, T. Li, S. Wang, B. Yang, A. L. Beck, R. D. Dupuis, and J. C. Campbell, Appl. Phys. Lett. **76**, 924 (1999).

[16] A. Osinsky, M. S. Shur, R. Gaska, and Q. Chen, Electron. Lett. **34**, 691 (1998).